

RESEARCH ARTICLE

Deep convolutional recurrent autoencoders for learning low-dimensional feature dynamics of fluid systems

Francisco J. Gonzalez* | Maciej Balajewicz

Department of Aerospace Engineering,
University of Illinois at Urbana-Champaign,
Urbana, Illinois, USA

Correspondence

*Francisco J. Gonzalez, Department of
Aerospace Engineering, University of
Illinois at Urbana-Champaign, Urbana,
Illinois, USA Email: ffgonza2@illinois.edu

Summary

Model reduction of high-dimensional dynamical systems alleviates computational burdens faced in various tasks from design optimization to model predictive control. One popular model reduction approach is based on projecting the governing equations onto a subspace spanned by basis functions obtained from the compression of a dataset of solution snapshots. However, this method is intrusive since the projection requires access to the system operators. Further, some systems may require special treatment of nonlinearities to ensure computational efficiency or additional modeling to preserve stability. In this work we propose a deep learning-based strategy for nonlinear model reduction that is inspired by projection-based model reduction where the idea is to identify some optimal low-dimensional representation and evolve it in time. Our approach constructs a modular model consisting of a deep convolutional autoencoder and a modified LSTM network. The deep convolutional autoencoder returns a low-dimensional representation in terms of coordinates on some expressive nonlinear data-supporting manifold. The dynamics on this manifold are then modeled by the modified LSTM network in a computationally efficient manner. An offline unsupervised training strategy that exploits the model modularity is also developed. We demonstrate our model on three illustrative examples each highlighting the model's performance in prediction tasks for fluid systems with large parameter-variations and its stability in long-term prediction.

KEYWORDS:

nonlinear model reduction, deep learning, convolutional neural networks, LSTM, dynamical systems

1 | INTRODUCTION

Dynamical systems are used to describe the rich and complex evolution of many real-world processes. Modeling the dynamics of physical, engineering, and biological systems is thus of great importance in their analysis, design, and control. Many fields, such as the physical sciences, are in the fortunate position of having a first-principles models that describes the evolution of certain systems with near-perfect accuracy (e.g., the Navier-Stokes equations in fluid mechanics, or Schrödingers equations in quantum mechanics). Although, in principle it is possible to numerically solve these equations through direct numerical simulations (DNS), this often yields systems of equations with millions or billions of degrees of freedom. Even with recent advances in computational power and memory capacity, solving these high-fidelity models (HFM) is still computationally intractable for *multi-query* and *time-critical* applications such as design optimization, uncertainty quantification, and model predictive control.

Model reduction aims to alleviate this burden by constructing reduced order models (ROMs) that capture the large-scale system behavior while retaining physical fidelity.

Some fields, however, such as finance and neuroscience, lack governing laws thereby restricting the applicability of principled strategies for constructing low-order models. In recent years, the rise in machine learning and big data have driven a shift in the way complex spatiotemporal systems are modeled^{1,2,3,4,5}. The abundance of data have facilitated the construction of so called data-driven models of systems lacking high-fidelity governing laws. In areas where HFMs do exist, data-driven methods have become an increasingly popular approach to tackle previously challenging problems wherein solutions are *learned* from physical or numerical data^{6,7,8}.

In model reduction, machine learning strategies have recently been applied to many remaining challenges, including learning stabilizing closure terms in unstable POD-Galerkin models^{8,9}, and data-driven model identification for truncated generalized POD coordinates^{10,11,12}. A more recent approach involved learning a set of observable functions spanning a Koopman invariant subspace from which low-order linear dynamics of nonlinear systems are modeled¹³. These approaches constitute just a small portion of the outstanding challenges in which machine learning can aid in modeling low-dimensional dynamics of complex systems.

In this work we make progress to this end by proposing a method that uses a completely data-driven approach to identify and evolve a low-dimensional representation of a spatiotemporal system. In particular, we employ a deep convolutional autoencoder to learn an optimal low-dimensional representation of the full state of the system in the form of a feature vector, or coordinates of some low-dimensional nonlinear manifold. The dynamics on this manifold are then learned using a recurrent neural network trained jointly with the autoencoder in an end-to-end fashion using a set of finite-time trajectories of the system.

1.1 | Reduced order and surrogate modeling

Model order reduction is part of a broader family of surrogate modeling strategies that attempt to reduce the computational burden of solving HFMs by instead solving approximate, low-complexity models. Surrogate models can be broadly classified into three groups: 1) data-fit models, 2) hierarchical models, and 3) projection-based model reduction^{14,15}. Data-fit models use simulation or experimental data to fit an input-output map as a function of system parameters. Some examples include models based on Gaussian processes^{1,16}, and feed-forward neural networks⁸. Hierarchical or low-fidelity models substitute the HFM with a lower-fidelity physics-based model that makes simplifying physics assumptions (e.g., ignoring viscous effects in a fluid flow), use coarser computational grids, or relaxes solver-tolerances.

In contrast to the first two surrogate modeling approaches, projection-based model reduction works by directly exploiting the low-dimensional behavior inherent in many high-dimensional dynamical systems. These methods approximate the state of the system by an affine trial subspace, and project the HFM onto a test subspace resulting in a square system of dimension much smaller than the original high dimension. Over the years, a large variety of empirically-based approaches for generating the trial and test subspaces have been developed, including proper orthogonal decomposition (POD)^{17,18}, Krylov subspace methods¹⁹, and dynamic mode decomposition²⁰. Despite the successes of projection-based model reduction, there exist a number of issues limiting the applicability of these methods.

One issue is that although the projection step effectively constrains the HFM to a lower dimensional subspace, this does not necessarily provide computational efficiency for general nonlinear models. Systems with generic, nonpolynomial nonlinearities or time-varying parameters require an additional layer of approximation, or *hyper-reduction*, to gain a computational speed up.[†] Some approaches for the treatment of nonlinearities include ROMs based on discrete empirical interpolation (DEIM)²¹, or Gauss-Newton with approximated tensors (GNAT)²². Other methods employ patchwork of local state space approximations at multiple locations including piecewise trajectory linearization (TPWL)²³ and ROMs based on trajectory piecewise quadratic (TPWQ) approximations²⁴. A second well known issue, particularly when dealing with high-Reynolds number fluid flows, is that of stability. POD-based ROMs are biased towards large energy-producing scales and are not endowed with the small energy-dissipating scales that maybe dynamically significant²⁵. Moreover, projection-based model reduction has the major disadvantage of being intrusive, requiring access to the system operators during the projection step. Thus, while optimal, say POD-based, approximations can be made of any dataset, the projection step is still limited to systems with existing governing laws.

[†]For linear time-invariant systems, or systems with polynomial nonlinearities all projection coefficient can be precomputed offline.

1.2 | Contributions and outline

In this work we develop a deep learning-based nonlinear model reduction strategy which is completely data-driven. This method employs a deep convolutional autoencoder to learn an optimal low-dimensional representation of each solution snapshot and later evolves this representation in time using a type of recurrent neural network (RNN) called a long short-term memory (LSTM) network. This work has important similarities to previous work using RNNs to evolve reduced order models^{10,12} and work that employs autoencoders for dimensionality reduction^{26,27,28,13}.

Although previous work regarding neural-network based reduced order models has shown great promise, a number of significant issues remain. Notably, while deep fully-connected autoencoders, such as the ones employed in^{13,27,28} work well for small systems with a few thousand degrees of freedom, this approach alone is not scalable as input data increases to DNS-level sizes (e.g., $10^6 - 10^9$ degrees of freedom (dof)). For example, an autoencoder just a single layer reducing input data from 10^6 dof to 100 will require training well over 10^8 parameters, a feat that quickly becomes computationally intractable as the autoencoder increases in depth.

To avoid this *curse of dimensionality*, we instead propose a convolutional recurrent autoencoding model that differs significantly from existing autoencoder-based model reduction approaches in two main ways:

- (i) We propose an autoencoding method that exploits local, location-invariant correlations present in physical data through the use of convolutional neural networks. That is, rather of applying a fully-connected autoencoder to the high-dimensional input data we instead apply it to a vectorized feature map produced by a convolutional encoder, and similarly the reverse is done for reconstruction. The result is the identification of an expressive low-dimensional manifold obtained at a much lower cost while offering specific advantages over both traditional POD-based ROMs and fully-connected autoencoders.
- (ii) We propose a modified LSTM network to model the evolution of low-dimensional data representations on this manifold that avoids costly state reconstructions at every step. In doing this, we ensure that the evaluation of new steps scales only with the size of the low-dimensional representation and not with the size of the full dimensional data, which may be large for some problems.

Taken together this end-to-end approach both identifies an optimal low-dimensional representation of a high-dimensional spatiotemporal dataset and models its dynamics on the underlying data-supporting manifold. Additionally a two-step unsupervised training strategy is developed that exploits the modularity of the convolution recurrent autoencoder model.

The paper is organized as follows. section 2 formulates the problem of interest and outlines the constraints underwhich our model is applied. section 3 briefly reviews the core concepts of deep learning used in this work, including recurrent and convolutional networks. A brief review of projection-based model reduction is also given in this section. Finally, we review the important connection between autoencoders and POD. The key contributions of this work are presented in section 4. Namely, the construction of the convolutional autoencoder for nonlinear dimensionality reduction and the construction of our modified LSTM network for modeling of feature dynamics. In this section, we also discuss the construction of the training datasets and develop our training strategy. section 5 demonstrates the use of our method on three illustrative examples. The first example considers a simple one-dimensional model reduction problem based on the viscous Burgers equation. This serves to highlight the expressive power of nonlinear autoencoders when compared to POD-based methods. Second, we consider a parametric model reduction problem based on an incompressible flow inside a periodic domain and evaluate our model's predictive performance with large parameter variations. This example has the merit of showcasing the benefits of the location-invariant properties of the convolutional autoencoder as compared to POD-based models. The last example highlights the stability characteristics of the convolutional recurrent autoencoder through a model reduction problem based on a chaotic incompressible flow inside a lid-driven cavity. Finally, section 6 presents a summary and discussion of our work.

2 | PROBLEM FORMULATION

2.1 | Nonlinear computational physics problem

Consider a high-dimensional ODE resulting from the semi-discretization of a time-dependent PDE

$$\begin{aligned}\dot{\mathbf{x}}(t) &= F(\mathbf{x}(t), t; \boldsymbol{\mu}), \\ \mathbf{x}(t_0) &= \mathbf{x}_0(\boldsymbol{\mu}),\end{aligned}\tag{1}$$

where $t \in [t_0, T] \subset \mathbb{R}^+$ denotes time, $\mathbf{x} \in \mathbb{R}^N$ is the spatially discretized state variable where N is large, and $\boldsymbol{\mu} \in \mathcal{D} \subseteq \mathbb{R}^d$ is the vector of parameters sampled from the feasible parameter set \mathcal{D} . Here, $F : \mathbb{R}^N \times \mathbb{R}^+ \times \mathbb{R}^d \rightarrow \mathbb{R}^N$ is a nonlinear function representing the dynamics of the discretized system. Such large nonlinear systems are typical in the computational sciences such as when numerically solving the Navier-Stokes equations describing a fluid flow. In the parameter-varying case $\boldsymbol{\mu}$ may represent initial and boundary conditions, material properties, or shape parameters of interest.

Often, in engineering design and analysis the interest is on the evolution of certain outputs

$$\mathbf{y} = G(\mathbf{x}(t), \boldsymbol{\mu}), \quad (2)$$

where $\mathbf{y} \in \mathbb{R}^p$ may represent e.g., lift, drag, or some other performance criteria. In this work, the attention is focused only on the evolution of the full state \mathbf{x} .

2.2 | Completely data-driven model reduction

When the number of degrees of freedom N is large, evaluating Equation 1 for a given initial condition and input parameter $\boldsymbol{\mu}$ becomes computationally challenging in two particular applications. The first are *time-critical* applications, or applications where a solution needs to be attained within a given threshold of time. Some examples include routine analysis applications and model predictive control of distributed parameter systems where near-real time solutions are crucial. The second are *multi-query* applications, i.e., applications where one needs to sample a large number of parameters from \mathcal{D} . Examples of multi-query applications include shape optimization and uncertainty quantification.

To alleviate this computational burden an offline-online strategy is usually employed in which a dataset of solution snapshots $\mathcal{X} = \{\mathbf{x}(t_i; \boldsymbol{\mu}_i)\}_{i=1}^{N_{\text{data}}}$ of Equation 1 is used to construct a surrogate model that is capable of approximating new solutions at a fraction of the cost. A wide variety of strategies exist for constructing these so-called data-driven models including data-fit methods which use numerical or experimental data to fit an input-output map, and projection-based reduced order models which approximately solve Equation 1 in a reduced subspace constructed from numerical or experimental data.

While projection-based reduced order models are physics-based, and thus offer an advantage over data-fit methods when it comes to physical interpretation, they are often intrusive. That is one requires access to the operators when performing the projection step. In this work, we will restrict our attention to non-intrusive, purely data-driven reduced order modeling. Thus, the construction of the surrogate model will require only the dataset \mathcal{X} and no information about Equation 1. Indeed there are many situations, e.g. in neuroscience and finance, in which data are abundant but governing laws are uncertain or do not exist altogether. For the purposes of this work, we will work under the assumption that we do not have access to Equation 1 from which the datasets are generated.

2.3 | Single vs. multiple parameter-varying trajectories

The construction and availability of solution snapshot datasets is inherently problem dependent. Here, we focus on the two common cases encountered in model reduction:

- (i) The dataset $\mathcal{X} = \{\mathbf{x}(t_1; \boldsymbol{\mu}), \mathbf{x}(t_2; \boldsymbol{\mu}), \dots\}$ is constructed using snapshots from a single, statistically stationary trajectory of Equation 1. In this case, $\boldsymbol{\mu}$ is the same for all snapshots. This is relevant to situations in which obtaining snapshot data is exceedingly expensive such as in large direct numerical simulations and the interest is on obtaining “quick” approximate solutions.
- (ii) The dataset $\mathcal{X} = \{X^{\mu_1}, X^{\mu_2}, \dots\}$ is constructed using multiple, parameter varying trajectories $X^{\mu_i} = \{\mathbf{x}(t_1; \boldsymbol{\mu}_i), \mathbf{x}(t_2; \boldsymbol{\mu}_i), \dots\}$. This case is relevant to multi-query applications or applications in which the interest is on capturing the parameter-dependent transient behavior of Equation 1.

In both cases the surrogate model is constructed in a non-intrusive fashion using the same procedure and only the dataset is changed.

3 | BACKGROUND

In this section, we introduce the basic notions of deep learning and two key architectures used in this work: 1) recurrent neural networks, and 2) convolutional neural networks. Finally, we finish by summarizing the connections between POD and fully-connected autoencoders.

3.1 | Deep learning

Deep learning has enjoyed great success in recent years in areas from image and speech recognition^{29,30,31} to genomics^{32,33}. At the core of deep learning are deep neural networks, whose layered structure allows them to learn at each layer a representation of the raw input with increasing levels of abstraction^{34,35}. With enough layers, deep neural networks can learn intricate structures in high-dimensional data. For example, given an image as an array of pixel values, the first layer of a deep neural network might learn to identify edges in various orientations. The second layer then is able to detect particular arrangements of edges, and so on until a complex hierarchy of features leads to the detection of a face or a road sign. Here, we briefly review some concepts and common network architectures used in this work.

Neural networks are models of computation loosely inspired by biological neurons. Generally, given a vector of real-valued inputs $\mathbf{x} \in \mathbb{R}^N$, a single layer artificial neural network is an affine transformation of the input \mathbf{x} fed through a nonlinear function

$$\hat{\mathbf{y}} = f(\mathbf{W}\mathbf{x} + \mathbf{b}), \quad (3)$$

where $\mathbf{W} \in \mathbb{R}^{M \times N}$ is the weight matrix, $\mathbf{b} \in \mathbb{R}^M$ is a bias term, and $f(\cdot)$ is a nonlinear function that acts element-wise on its inputs.

To create multilayered neural networks, the output \mathbf{h}_l of a layer l is fed as the input of the following layer, thus

$$\begin{aligned} \mathbf{h}_{l+1} &= f_{l+1}(\mathbf{W}_l \mathbf{h}_l + \mathbf{b}_l), \\ &= f_{l+1}(\mathbf{W}_l f_l(\dots(f_1(\mathbf{W}_0 \mathbf{x} + \mathbf{b}_0))\dots + \mathbf{b}_{l-1}) + \mathbf{b}_l), \end{aligned} \quad (4)$$

where $\mathbf{h}_1 = f_1(\mathbf{W}_0 \mathbf{x} + \mathbf{b}_0)$ is the output of the first layer. The vector \mathbf{h}_l is often referred to as the hidden state or feature vector at the l -th layer. This process continues for L layers, where at the final layer the output of the network is given by $\hat{\mathbf{y}} = f_L(\mathbf{W}_{L-1} \mathbf{h}_{L-1} + \mathbf{b}_{L-1})$. In supervised learning, training the network then involves finding the parameters $\theta = \{\mathbf{W}_l, \mathbf{b}_l\}_{l=0}^{L-1}$ such that the expected loss between the output $\hat{\mathbf{y}}$ and the target value \mathbf{y} is minimized

$$\theta^* = \arg \min_{\theta} \mathbb{E}_{(\mathbf{x}, \mathbf{y}) \sim \mathcal{P}_{data}} [\mathcal{L}(f(\mathbf{x}; \theta), \mathbf{y})], \quad (5)$$

where \mathcal{P}_{data} is the data-generating distribution and $\mathcal{L}(\hat{\mathbf{y}}, \mathbf{y})$ is some measure of discrepancy between the predicted and target outputs. What distinguishes machine learning from straight forward optimization is that the model f parameterized by θ^* should be expected to generalize well for all examples drawn from \mathcal{P}_{data} , even if they were not witnessed during training³⁴. Most neural networks are trained using stochastic gradient descent (SGD), or one of its many variants^{36,37}, in which gradients are computed using the backpropagation procedure³⁸.

3.2 | Recurrent neural networks

A natural extension of feed-forward networks for sequential data are networks with self-referential, or recurrent connection. These recurrent neural networks (RNNs) process a sequence of inputs one element at a time, maintaining in the hidden state an implicit history of previous inputs. Consider a sequence of inputs $\{\mathbf{x}^0, \mathbf{x}^1, \dots, \mathbf{x}^m\}$, with each $\mathbf{x}^n \in \mathbb{R}^N$, the n -th hidden state $\mathbf{h}^n \in \mathbb{R}^{N_h}$ of a simple RNN is evaluated by the following update

$$\mathbf{h}^n = f(\mathbf{W}\mathbf{h}^{n-1} + \mathbf{U}\mathbf{x}^n + \mathbf{b}), \quad (6)$$

where $\mathbf{W} \in \mathbb{R}^{N_h \times N_h}$ and $\mathbf{U} \in \mathbb{R}^{N_h \times N}$ are the hidden and input weight matrices respectively, and $\mathbf{b} \in \mathbb{R}^{N_h}$ is a bias term. RNNs are also typically trained using SGD, or some variant, but the gradients are calculated using the backpropagation through time (BPTT) algorithm³⁹. In BPTT, the RNN is first “unrolled” in time, stacking one copy of the RNN per time step. This results in a *weight-tied* deep feed forward neural network on which the standard backpropagation algorithm can be employed.

Training RNNs has long been considered to be challenging⁴⁰. The main difficulty is due to the exponential growth or decay of gradients as they are backpropagated through each time step, so over many time steps they will either vanish or explode. This is especially problematic when learning sequences with long-term dependencies. The vanishing or exploding gradient

problem is typically addressed by using gated RNNs, including long short-term memory (LSTM) networks⁴¹ and networks based on the gated recurrent unit (GRU)⁴². These networks have additional paths through which gradients neither vanish nor explode, allowing gradients of the loss function to backpropagate across multiple time-steps and thereby making the appropriate parameter updates. This work will only consider RNNs equipped with LSTM units.

3.3 | Convolutional neural networks

The final standard neural network architecture considered in this work are convolutional neural networks. These networks were first introduced as an alternative to fully connected networks for data structured as multiple arrays (e.g., 1D signals and sequences, 2D images or spectrograms, and 3D video). The two key properties of convolutional neural networks are: 1) local connections, and 2) shared weights^{34,35}. In arrayed data, often local groups of values are highly correlated, assembling into distinct features that can be easily detected using a local approach. Additionally, weight sharing across the input domain works to detect location-invariant features.

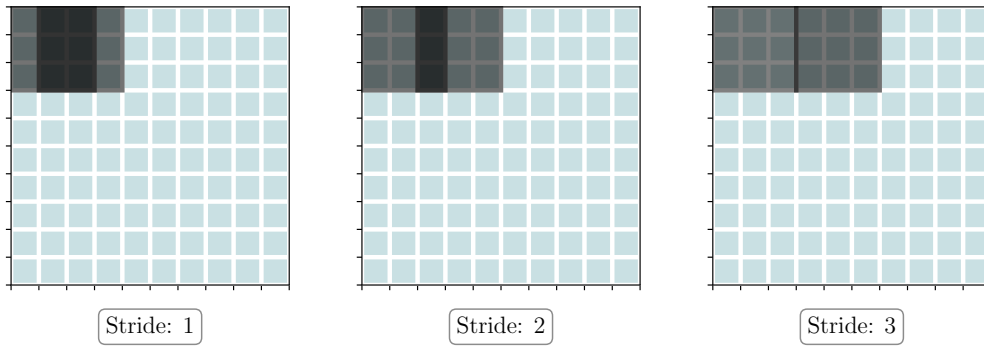


FIGURE 1 Sliding convolutional filter with varying stride values.

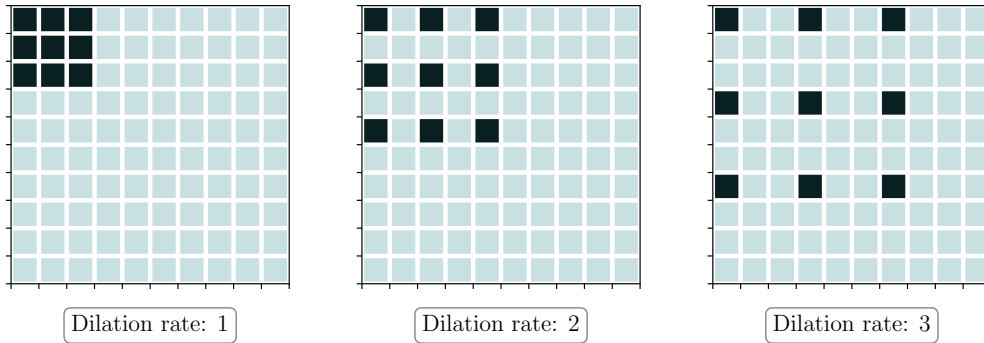


FIGURE 2 Convolutional filters with varying dilation rates.

In convolutional neural networks, layers are organized into feature maps, where each unit in a feature map is connected to a local domain of the previous layer through a filter bank. Consider a 2D input $\mathbf{X} \in \mathbb{R}^{N_x \times N_y}$, a convolutional layer consists of a set of F filters $\mathbf{K}^f \in \mathbb{R}^{a \times b}$, $f = 1, \dots, F$, each of which generates a feature map $\mathbf{Y}^f \in \mathbb{R}^{N'_x \times N'_y}$ by a 2D discrete convolution

$$\mathbf{Y}_{i,j}^f = \sum_{k=0}^{a-1} \sum_{l=0}^{b-1} \mathbf{K}_{a-k,b-l}^f \mathbf{X}_{1+s(i-1)-k, 1+s(j-1)-l}, \quad (7)$$

where $N'_x = 1 + \frac{N_x + a - 2}{s}$, $N'_y = 1 + \frac{N_y + b - 2}{s}$, and $s \geq 1$ is an integer value called the *stride*. Figure 1 shows the effect of different stride values of a filter acting on an input feature map. As before, the feature map can be passed through an element-wise nonlinear function. Typically, the dimension of the feature map is reduced by using a pooling layer, in which a single value is computed from small $a' \times b'$ patch of the feature map either by taking the maximum value or averaging. A slightly more general approach is to employ a convolutional layer with a stride of $s > 1$, in which instead of taking the maximum or average value, some weighted sum of the local patch of the input feature map is learned by adjusting the respective filter \mathbf{K}^f . In addition, dilated convolutional filters (see Figure 2) are often employed to significantly increase the receptive field without loss of resolution, effectively capturing larger features in highly dense data^{43,44}.

3.4 | Projection-based model reduction

In projection-based MOR, the state vector $\mathbf{x} \in \mathbb{R}^N$ is approximated by a global affine trial subspace $\mathbf{x}^0 + S \subset \mathbb{R}^N$ of dimension $N_h \ll N$

$$\mathbf{x} \approx \tilde{\mathbf{x}} = \mathbf{x}^0 + \Psi_{N_h} \mathbf{h}, \quad (8)$$

where the columns of $\Psi_{N_h} \in \mathbb{R}^{N \times N_h}$ contain the basis for subspace S , the initial condition is given by \mathbf{x}^0 , and $\mathbf{h} \in \mathbb{R}^{N_h}$ represents the generalized coordinates in this subspace. Substituting Equation 8 into Equation 1 yields

$$\Psi_{N_h} \frac{d\mathbf{h}}{dt} = F(\mathbf{x}^0 + \Psi_{N_h} \mathbf{h}(t; \mu)), \quad (9)$$

which is an overdetermined system with N equations and N_h unknowns. Additional constraints are imposed by enforcing the orthogonality of the residual of Equation 9 on a test subspace represented by $\Phi \in \mathbb{R}^{N \times N_h}$ through a Petrov-Galerkin projection

$$\Phi^T R(\mathbf{x}^0 + \Psi_{N_h} \mathbf{h}(t; \mu)) = 0, \quad (10)$$

resulting in a square system with N_h equations and N_h unknowns, where $R(\cdot)$ represents the residual of Equation 9. In a Galerkin projection, $\Phi = \Psi_{N_h}$. An important task is now choosing the subspace S on which to project the governing equation Equation 1. One popular method is to obtain the basis of S through proper orthogonal decomposition (POD).[‡]

Beginning with a set of m observations $\{\mathbf{x}^n\}_{n=1}^m$, $\mathbf{x}^n \in \mathbb{R}^N$, formed into a data matrix $\mathbf{X} = [\mathbf{x}^1, \mathbf{x}^2, \dots, \mathbf{x}^m] \in \mathbb{R}^{N \times m}$, POD consists of performing the singular value decomposition (SVD) on this data matrix

$$\mathbf{X} = \Psi \Sigma \mathbf{V}^T, \quad (11)$$

where $\Psi \in \mathbb{R}^{N \times r}$ and $\mathbf{V} \in \mathbb{R}^{m \times r}$ are orthonormal, i.e., $\Psi^T \Psi = \mathbf{V}^T \mathbf{V} = \mathbf{I}_{r \times r}$, and $\Sigma \in \mathbb{R}^{r \times r}$ is a diagonal matrix of whose entries $\sigma_i \geq 0$, ordered as $\sigma_1 \geq \sigma_2 \geq \dots \geq \sigma_r$ are the singular values. The columns ψ_i of Ψ are sometimes called the principal components, features, or POD modes. These modes have the property that the linear subspace S spanned by $\Psi_{N_h} = [\psi_1, \dots, \psi_{N_h}]$, $N_h < r$, optimally represents the data in the L_2 sense

$$\min_{\Psi_{N_h}} \|\mathbf{X} - \Psi_{N_h} \Psi_{N_h}^T \mathbf{X}\|_2^2 = \min_{\Psi_{N_h}} \sum_{i=1}^m \|\mathbf{x}_i - \Psi_{N_h} \Psi_{N_h}^T \mathbf{x}_i\|_2^2. \quad (12)$$

The net result is an optimal low-dimensional representation $\mathbf{h} = \Psi_{N_h}^T \mathbf{x}$ of an input \mathbf{x} , where again \mathbf{h} can be thought of as the intrinsic coordinates on the linear subspace S .

3.5 | Connection between autoencoders and POD

In data-driven sciences, dimensionality reduction attempts to approximately describe high-dimensional data in terms of a low-dimensional representation. Central to this is the *manifold hypothesis*, which presumes that real-world high-dimensional data lies near a low-dimensional manifold S embedded in \mathbb{R}^N , where N is large⁴⁵. As a result POD has found broad applications from pre-training machine learning models to dimensionality reduction of physical systems. However it has the major drawback of constructing only an optimal linear manifold. This is quite significant since data sampled from complex, real-world systems is more often than not strongly nonlinear. A wide variety of strategies for more accurate modeling of S have been developed

[‡]This method is known under different names in various fields: POD, principal component analysis (PCA), Karhunen-Loève decomposition, empirical orthogonal functions and many others. In this work we will adopt the name POD.

over the years, most involving using a patchwork of local subspaces $\{S_l\}_{l=1}^L$ obtained through linearizations or higher-order approximations of the state-space^{23,45,24}.

A nonlinear generalization of POD is the under-complete autoencoder^{26,34}. An under-complete autoencoder consists of a single or multiple-layer *encoder* network

$$\mathbf{h} = f_E(\mathbf{x}; \theta_E), \quad (13)$$

where $\mathbf{x} \in \mathbb{R}^N$ is the input state, $\mathbf{h} \in \mathbb{R}^{N_h}$ is the feature or representation vector, and $N_h < N$. A *decoder* network is then used to reconstruct \mathbf{x} by

$$\hat{\mathbf{x}} = f_D(\mathbf{h}; \theta_D). \quad (14)$$

Training this autoencoder then consists of finding the parameters that minimize the expected reconstruction error over all training examples

$$\theta_E^*, \theta_D^* = \arg \min_{\theta_E, \theta_D} \mathbb{E}_{\mathbf{x} \sim \mathcal{P}_{data}} [\mathcal{L}(\hat{\mathbf{x}}, \mathbf{x})], \quad (15)$$

where $\mathcal{L}(\hat{\mathbf{x}}, \mathbf{x})$ is some measure of discrepancy between \mathbf{x} and its reconstruction $\hat{\mathbf{x}}$. Restricting $N_h < N$ serves as a form of regularization, preventing the autoencoder from learning the identity function. Rather, it captures the salient features of the data-generating distribution \mathcal{P}_{data} . Under-complete autoencoders are just one of a family of regularized autoencoders which also include contractive autoencoders, denoising autoencoders, and sparse autoencoders^{26,34}.

Remark 1. The choice of f_E , f_D , and $\mathcal{L}(\hat{\mathbf{x}}, \mathbf{x})$ largely depends on the application. Indeed, if one chooses a linear encoder and a linear decoder of the form

$$\mathbf{h} = \mathbf{W}_E \mathbf{x}, \quad (16)$$

$$\hat{\mathbf{x}} = \mathbf{W}_D \mathbf{h}, \quad (17)$$

where $\mathbf{W}_E \in \mathbb{R}^{N_h \times N}$ and $\mathbf{W}_D \in \mathbb{R}^{N \times N_h}$, then with a squared reconstruction error

$$\begin{aligned} \mathcal{L}(\hat{\mathbf{x}}, \mathbf{x}) &= \|\mathbf{x} - \hat{\mathbf{x}}\|_2^2 \\ &= \|\mathbf{x} - \mathbf{W}\mathbf{W}^T \mathbf{x}\|_2^2, \end{aligned} \quad (18)$$

the autoencoder will learn the same subspace as the one spanned by the first N_h POD modes if $\mathbf{W} = \mathbf{W}_D = \mathbf{W}_E^T$. However, without additional constraints on \mathbf{W} , i.e., $\mathbf{W}^T \mathbf{W} = \mathbf{I}_{N_h \times N_h}$, the columns of \mathbf{W} will not form an orthonormal basis or have any hierarchical ordering^{45,46}.

4 | CONVOLUTIONAL RECURRENT AUTOENCODERS FOR MODEL REDUCTION

4.1 | Previous work and objectives

In the past few years machine learning has become an increasingly attractive tool in modeling or augmenting low-dimensional models of complex systems. Broadly, machine learning has been used in three ways in this respect: 1) as input-output maps to model closure terms in unstable POD-Galerkin models, 2) as a means to model the evolution of the intrinsic coordinates from an optimal subspace approximation of the state, and more recently 3) as an approach to construct end-to-end models that both find optimal representations of the system variables and linearly evolve these representations. Our work was motivated and thus has important similarities to previous work in both the second and third approach.

The main idea behind modeling the evolution of the optimal subspace approximations of the state variable directly addresses one of the main challenges of projection-based model reduction. Namely, for systems where governing laws do not exist, a simple yet powerful approach is to model the evolution the intrinsic coordinates, obtained for example through POD, using of a recurrent neural network

$$\mathbf{h}^{n+1} = f_{RNN}(\mathbf{h}^n), \quad (19)$$

where the representation vector $\mathbf{h} \in \mathbb{R}^{N_h}$, is of much lower dimension than the data from which it is approximated. This strategy has previously been explored in the context of model reduction where \mathbf{h} is obtained through POD^{12,10}, and in the more general case where Equation 19 may model the dynamic behavior of complex⁴⁷ or chaotic systems⁴⁸. This opens up a family of strategies for modeling the dynamics of not just systems without HFM, but systems with heterogeneous data sources, and systems with *a priori* unknown optimal subspace approximations – a feature which we make use of in this work.

A more completely data-driven approach, and one that is more closely related to our work, is to both learn a low-dimensional representation of the state variable and to learn the evolution of this representation. This approach has been explored in ¹³ in which an autoencoder is used to learn a low-dimensional representation of the high-dimensional state,

$$\mathbf{h} = f_E(\mathbf{x}), \quad (20)$$

where $\mathbf{x} \in \mathbb{R}^N$ high-dimensional state of the system, $\mathbf{h} \in \mathbb{R}^{N_h}$, $N_h < N$, and a linear recurrent model is used to evolve the low-dimensional features

$$\mathbf{h}^{n+1} = \mathbf{K}\mathbf{h}^n, \quad (21)$$

where $\mathbf{K} \in \mathbb{R}^{N_h \times N_h}$. This approach was first introduced in the context of learning a dictionary of functions used in extended dynamic mode decomposition to approximate the Koopman operator of a nonlinear system ⁴⁹.

The central theme in these approaches and projection-based model reduction in general is the following two-step process:

1. The identification of a low-dimensional manifold S embedded in \mathbb{R}^N on which most of the data is supported. This yields, in some sense, an optimal low-dimensional representations $\mathbf{h} = f(\mathbf{x})$ of the data \mathbf{x} in terms of intrinsic coordinates on S , and
2. The identification of a dynamic model which efficiently evolves the low-dimensional representation \mathbf{h} on the manifold S .

In this work, we build on the framework introduced in ^{10,12,13} for constructing or augmented reduced order models, and extend it in multiple directions. First, we introduce a deep convolutional autoencoder architecture which provides certain advantages in identifying low-dimensional representation of the input data. Second, since the dynamics of reduced state vector on S may not necessarily be linear, we employ a single-layer LSTM network to model the possibly nonlinear evolution of \mathbf{h} on S . Lastly, we introduce an unsupervised training strategy which trains the convolutional autoencoder while using the current reduced state vectors to dynamically train the LSTM network.

4.2 | Dimensionality reduction via convolutonal autoencoders

Dimensionality reduction through fully-connected autoencoders have long been used in a wide variety of applications. However, one quickly runs into the *curse of dimensionality* when considering DNS-level input data which can easily reach 10^9 dof as mentioned in the introduction. Directly applying large physical or simulation data to fully-connected autoencoders is not only computationally prohibitive, but the approach itself ignores the opportunity to exploit the structure of features in high-dimensional data. That is, since fully-connected autoencoders require that the input data be flattened into an 1D array, the local spatial relations between values are eliminated and can only be recovered by initially considering dense models. Sparsity can be achieved either *a posteriori* by pruning individual connections (setting $w_{ij} = 0$ for some i, j) after training, or encouraged during training by using L_1 regularization. Here, we seek to exploit local correlations present in many physics-based data through the use of convolutional neural networks.

In particular, rather than applying a fully-connected autoencoder directly to complex, high-dimensional simulation or experimental data, we apply it to a vectorized feature map of a much lower-dimension obtained from a deep convolutional network acting directly on the high-dimensional data. Wrapping the fully-connected autoencoder with a convolutional neural network has two significant advantages:

- (i) The local approach of each convolutional layer helps to exploit local correlations in field values. Thus, much the same way finite-difference stencils can capture local gradients, each filter \mathbf{K}^f in a filter bank computes local low-level features from a small subset of the input.
- (ii) The shared nature of each filter bank both allows to identify similar features throughout the input domain and reduce the overall number of trainable parameters compared to a fully-connected layer with the same input size.

Consider the following 12-layer convolutional autoencoder model depicted graphically in Figure 3. A 2D arrayed input $\mathbf{X} \in \mathbb{R}^{N_x \times N_y}$, with $N_x = N_y = 128$, is first passed through 4-layer convolutional encoder. Each convolutional encoder layer uses a filter bank $\mathbf{K}^f \in \mathbb{R}^{5 \times 5}$, with the first layer having a dilation rate of 2 and the number of filters f increasing from 4 in the first layer to 32 in the fourth layer using Equation 7. At the opposite end of the convolutional autoencoder network we use a 4-layer decoder network consisting of *transpose* convolutional layers. Often erroneously referred to as “deconvolutional”

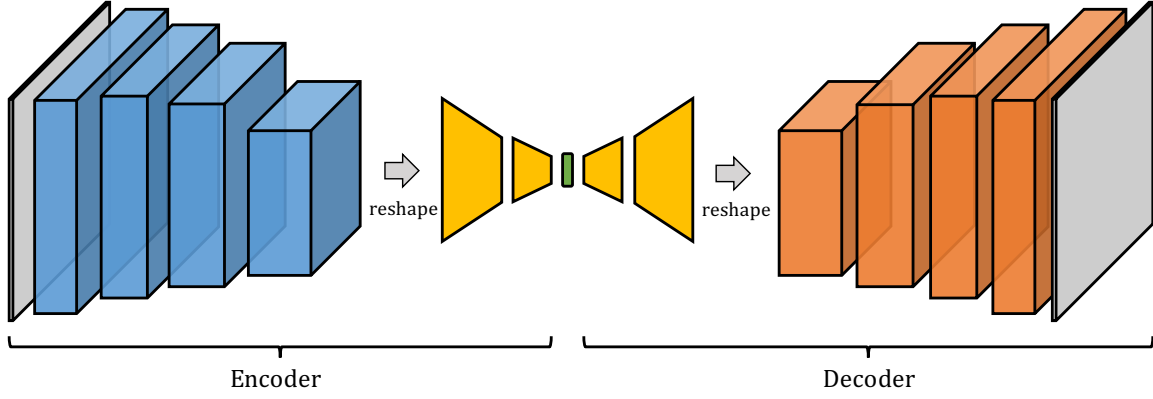


FIGURE 3 Network architecture of the convolutional autoencoder. The encoder network consists of a 4-layer convolutional encoder (blue), a 4-layer fully-connected encoder and decoder (yellow), and a 4-layer transpose convolutional decoder (red). The low-dimensional representation is depicted in green.

layers, transpose convolutional layers multiply each element of the input with a filter \mathbf{K}^f and sum over the resulting feature map, effectively swapping the forward and backward passes of a regular convolutional layer. The effect of using transpose convolutional layers with a stride $s > 1$ is two decode low-dimensional abstract features to a larger dimensional representation. Table 1 outlines the architecture of the convolutional encoder and decoder subgraphs. In this work will consider the sigmoid activation function $\sigma(s) = 1 / (1 + \exp(-s))$ for each layer of the autoencoder.[§]

TABLE 1 Convolutional encoder (left) and decoder (right) filter sizes and strides

Layer	filter size	filters	stride	Layer	filter size	filters	stride
1	5×5	4	2×2	9	5×5	16	2×2
2	5×5	8	2×2	10	5×5	8	2×2
3	5×5	16	2×2	11	5×5	4	2×2
4	5×5	32	2×2	12	5×5	1	2×2

In between the convolutional encoder and decoder is a regular fully-connected autoencoder consisting of a 2-layer encoder which takes the vectorized form of the 32 feature maps from the last convolutional encoder layer $\text{vec}(\mathcal{Y}) \in \mathbb{R}^{512}$, where $\mathcal{Y} = [\mathbf{Y}^1, \dots, \mathbf{Y}^{32}] \in \mathbb{R}^{4 \times 4 \times 32}$, and returns the final low-dimensional representation of the input data

$$\mathbf{h} = \sigma(\mathbf{W}_E^2 \sigma(\mathbf{W}_E^1 \text{vec}(\mathcal{Y}) + \mathbf{b}_E^1) + \mathbf{b}_E^2) \in \mathbb{R}^{N_h}, \quad N_h \ll (N_x \cdot N_y), \quad (22)$$

where $\mathbf{W}_E^1, \mathbf{b}_E^1$ and $\mathbf{W}_E^2, \mathbf{b}_E^2$ are the parameters of the first and second fully-connected encoder network (the 5th and 6th layers of the whole model). To reconstruct the original input data from the low-dimensional representation, a similar 2-layer fully-connected decoder parameterized by $\mathbf{W}_D^1, \mathbf{b}_D^1$ and $\mathbf{W}_D^2, \mathbf{b}_D^2$, whose result is reshaped and passed to the transpose convolutional decoder network.

Hierarchical convolutional feature learning through similar strategies have previously been proposed for visual tracking⁵¹ and scene labeling or semantic segmentation of images^{30,52,53}. However, this is the first time, to the authors knowledge, that a convolutional autoencoders have been applied to model reduction of large numerical data of physical dynamical systems. The key innovation in using convolutional autoencoders in model reduction is that it allows for nonlinear autoencoders and thus nonlinear model reduction to be applied to large input data in a way that exploits structures inherent in many physical systems.

[§]In recent years the rectified linear units (ReLU)s³⁴, given by $\text{ReLU}(s) = \max(0, s)$, and its many variants like the ELUs⁵⁰, have been favored over the sigmoid activation function. However, in this work we have found that ReLUs produce results similar to linear model reduction theory since $\text{ReLU}(s)$ are linear for inputs $s \in \mathbb{R}^+$.

Remark 2. In this work we restrict our attention to 2D input data of size $N_x \times N_y = 128 \times 128$ with the first layer convolutional filter having a dilation rate of 2. In practice, however, an equivalent memory-reducing approach was employed by using an input data of size $N_x \times N_y = 64 \times 64$. In addition, the low-dimensional representations considered in this work are of size $N_h = 64$ or smaller. To this effect, the hidden state sizes of the middle fully-connected autoencoder were chosen to be 512 and 256 such that $\mathbf{W}_E^1, (\mathbf{W}_D^2)^T \in \mathbb{R}^{512 \times 256}$ and $\mathbf{W}_E^2, (\mathbf{W}_D^1)^T \in \mathbb{R}^{256 \times N_h}$ with the bias terms shaped accordingly. The net result is an autoencoder with a maximum of 330k parameters with $N_h = 64$. A similar 12-layer fully-connected autoencoder would require over 22M parameters.

Remark 3. The size of the low-dimensional representation N_h must be chosen *a priori* for each model. Currently, no principled approach exists for the choice of N_h . One possible heuristic for an upper bound is to choose N_h such that

$$\frac{\sum_{i=1}^{N_h} \sigma_i^2}{\sum_{i=1}^m \sigma_i^2} < \kappa, \quad (23)$$

where $\sigma_i \geq 0$ are the singular values of the data matrix $\mathbf{X} \in \mathbb{R}^{N \times m}$ and κ is usually taken to be 99.9%. This approach is often employed when selecting the number of POD modes to keep in POD-Galerkin reduced order models¹⁴, where in the context of fluid flows this corresponds to choosing enough modes such that 99.9% of the energy content in the flow is preserved.

4.3 | Learning feature dynamics

The second component of projection-based model reduction is modeling the evolution of low-dimensional features \mathbf{h} in a computationally efficient manner. Though identifying linear dynamics of \mathbf{h} is beneficial from an analysis perspective, here we will consider the general case of learning arbitrary feature dynamics.

Consider a set of observations $\{\mathbf{x}^n\}_{n=0}^m, \mathbf{x}^n \in \mathbb{R}^N$ obtained from a HFM or through experimental sampling. Furthermore, for each observations consider some optimal low-dimensional representation $\mathbf{h}^n \in \mathbb{R}^{N_h}$, where $N_h \ll N$. This low-dimensional representation can come from an optimal rank- N_h POD representation $\mathbf{h}^n = \Psi_{N_h}^T \mathbf{x}^n$, where the columns of Ψ_{N_h} are the first N_h POD modes, or through a neural network approach such as an autoencoder. We seek to construct a model for the evolution of this low-dimensional representation in a completely data-driven fashion, i.e., without access or knowledge of the system operators. This is particularly useful for cases where HFM are uncertain or do not exist altogether.

To model the evolution of \mathbf{h} we employ a modified version of the long short term memory (LSTM) network. **LSTM networks we first proposed primarily to overcome the vanishing or exploding gradient problem and are equipped with an explicit memory cell and four gating units which adaptively control the flow of information through the network**^{41,54}. LSTM networks have demonstrated impressive results in modeling relationships between sequences such as in machine translation tasks^{55,42,56,35}. More recently, they have been used to predict conditional probability distributions in chaotic dynamical systems⁴⁸ and in modeling the evolution of low-dimensional POD representations^{10,12}.

In this work we are interested in evolving feature vectors whose size correspond to the intrinsic dimensionality of a physical system, which may be small compared to the number of hidden states and layers used in e.g., machine translation. In addition, for large-scale systems it may be inefficient, if not computationally prohibitive to reconstruct the full high-dimensional state at every time-step. With these restrictions, we construct a modified **single-layer LSTM** network to evolve the low-dimensional representation \mathbf{h}^n without full state reconstruction with the following components:

- *Input gate:*

$$\mathbf{i}^n = \sigma(\mathbf{W}_i \mathbf{h}^{n-1} + \mathbf{b}_i)$$

- *Forget gate:*

$$\mathbf{f}^n = \sigma(\mathbf{W}_f \mathbf{h}^{n-1} + \mathbf{b}_f)$$

- *Output gate:*

$$\mathbf{o}^n = \sigma(\mathbf{W}_o \mathbf{h}^{n-1} + \mathbf{b}_o)$$

- *Cell state:*

$$\mathbf{c}^n = \mathbf{i}^n \odot \mathbf{c}^{n-1} + \mathbf{i}^n \odot \tanh(\mathbf{W}_c \mathbf{h}^{n-1} + \mathbf{b}_c)$$

where all four gates are used to update the feature vector by

$$\mathbf{h}^n = \mathbf{o}^n \odot \tanh(\mathbf{c}^n). \quad (24)$$

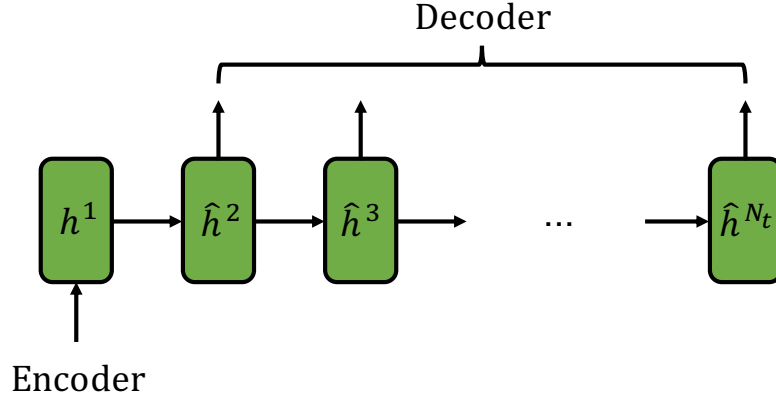


FIGURE 4 LSTM model that iteratively updates the low-dimensional representation \mathbf{h} .

Here, \odot represents the Hadamard product. Intuitively, at each step n the input and forget gates choose what information gets passed and dropped from the cell state \mathbf{c}^n , while the output gate controls the flow of information from the cell state to the feature vector. It is important to note that the evolution of \mathbf{h} does not require information from the full state \mathbf{x} , thereby avoiding a costly reconstruction at every step.

Initializing with a known low-dimensional representation \mathbf{h}^0 one obtains a prediction for the following steps by iteratively applying

$$\hat{\mathbf{h}}^{n+1} = f_{LSTM}(\hat{\mathbf{h}}^n) \quad n = 1, 2, 3, \dots \quad (25)$$

where $\hat{\mathbf{h}}^1 = f_{LSTM}(\mathbf{h}^0)$, and $f_{LSTM}(\cdot)$ represents the action of Equation 24 and its subcomponents. A graphical representation of this model is depicted in Figure 4.

4.4 | Unsupervised training strategy

A critical component of this work is the development of an unsupervised training approach that adjusts both the convolutional autoencoder and recurrent model in a joint fashion. The main obstacle is in preventing either the convolutional autoencoder or RNN portion of the model from overfitting. Here, we discuss the construction of the training dataset as well as the training and evaluation algorithms.

4.4.1 | Constructing the training dataset

Consider a dataset $\{\mathbf{x}^1, \mathbf{x}^2, \dots, \mathbf{x}^m\}$, where $\mathbf{x} \in \mathbb{R}^{N_x \times N_y}$ is a 2D snapshot of some dynamical system (e.g., a velocity field defined on a 2D grid). To make this dataset amenable to training it is broken up into a set of N_s finite-time training sequences $\{\mathbf{X}^1, \dots, \mathbf{X}^{N_s}\}$, where each training sequence $\mathbf{X}^i \in \mathbb{R}^{N_x \times N_y \times N_t}$ consists of N_t snapshots. Parameter-varying datasets naturally break up in this form where each \mathbf{X}^i may represent a small sequence of snapshots corresponding to a single parameter value μ_i .

A common strategy for improving training is to consider only the fluctuations around the temporal mean

$$\mathbf{x}'^n = \mathbf{x}^n - \bar{\mathbf{x}}, \quad (26)$$

where $\bar{\mathbf{x}} = \frac{1}{m} \sum_{n=1}^m \mathbf{x}^n$ is the temporal average over the entire dataset and \mathbf{x}' are the fluctuations around this mean. In our case, each layer in the convolutional autoencoder uses the sigmoid activation function which maps each real-valued input to the interval $(0, 1)$, requiring our dataset be feature-scaled in order to prevent saturation of the activation³⁴. Thus, our training dataset consists of feature scaled snapshots

$$\mathbf{x}'_s{}^n = \frac{\mathbf{x}'^n - \mathbf{x}'_{min}}{\mathbf{x}'_{max} - \mathbf{x}'_{min}}, \quad (27)$$

where each $\mathbf{x}'_s{}^n \in [0, 1]^{N_x \times N_y}$. With these modifications, the resulting training dataset has the following form

$$\mathcal{X} = \{\mathbf{X}'_s{}^1, \dots, \mathbf{X}'_s{}^{N_s}\} \in [0, 1]^{N_x \times N_y \times N_t \times N_s}, \quad (28)$$

where each training sample $\mathbf{X}'_s{}^i = [\mathbf{x}'_{s,i}{}^1, \dots, \mathbf{x}'_{s,i}{}^{N_t}]$ is a matrix consisting of the feature-scaled fluctuations.

4.4.2 | Offline training and online prediction algorithms

Our approach to train both components of the convolutional recurrent autoencoder model is to split the forward pass into two stages. In the first stage, the autoencoder takes an N_b -sized batch of the training data $\mathcal{X}^b \subset \mathcal{X}$, where $\mathcal{X}^b \in [0, 1]^{N_x \times N_y \times N_t \times N_b}$, and outputs both the current N_b -sized batch of low-dimensional representations of the training sequence

$$\mathcal{H}^b = \{\mathbf{H}^1, \dots, \mathbf{H}^{N_b}\} \in \mathbb{R}^{N_h \times N_t \times N_b}, \quad (29)$$

where $\mathbf{H}^i = [\mathbf{h}_i^1, \dots, \mathbf{h}_i^{N_t}] \in \mathbb{R}^{N_h \times N_t}$ and a reconstruction $\hat{\mathcal{X}}^b$ of the original input training batch. In the second stage of the forward pass, the first feature vector of each sequence is used to initialize and iteratively update Equation 25 to get a reconstruction $\hat{\mathcal{H}}^b$ of the low-dimensional representations of the training batch Equation 28.

We seek to construct a loss function that equally weights the error in the full-state reconstruction and the evolution of the low-dimensional representations. In general, we would like to find the model parameters θ such that for any sequence $\mathbf{X}'_s = [\mathbf{x}'_s^1, \dots, \mathbf{x}'_s^{N_t}]$, $\mathbf{x}'_s^{n_t} \sim \mathcal{P}_{data}$ and its corresponding low-dimensional representation $\mathbf{H} = [\mathbf{h}^1, \dots, \mathbf{h}^{N_t}]$, where \mathcal{P}_{data} is the data-generating distribution, minimizes the following expected error between the model and the data

$$\begin{aligned} \mathcal{J}(\theta) &= \mathbb{E}_{\mathbf{x}'_s \sim \mathcal{P}_{data}} [\mathcal{L}(\hat{\mathbf{X}}'_s, \mathbf{X}'_s, \hat{\mathbf{H}}, \mathbf{H})] \\ &= \mathbb{E}_{\mathbf{x}'_s \sim \mathcal{P}_{data}} \left[\frac{\alpha}{N_t} \sum_{n=1}^{N_t} \frac{\|\mathbf{x}'_s^{n_t} - \hat{\mathbf{x}}_s^{n_t}\|_F^2}{\|\mathbf{x}'_s^{n_t}\|_F^2 + \epsilon} + \frac{\beta}{N_t - 1} \sum_{n=2}^{N_t} \frac{\|\mathbf{h}^n - \hat{\mathbf{h}}^n\|_2^2}{\|\mathbf{h}^n\|_2^2 + \epsilon} \right] \end{aligned} \quad (30)$$

where $\epsilon > 0$ is a small positive number and $\alpha = \beta = 0.5$. In practice, the expected error is approximated by averaging $\mathcal{L}(\hat{\mathbf{X}}'_s, \mathbf{X}'_s, \hat{\mathbf{H}}, \mathbf{H})$ over all samples in a training batch during each backward pass. Intuitively, at every training step, the autoencoder performs a regular forward pass while constructing a new batch of low-dimensional representations which are used to train the RNN. In this work we use the ADAM optimizer³⁶, a version of stochastic gradient descent that computes adaptive learning rates for different parameters using estimates of first and second moments of the gradients. Algorithm 4.1 outlines the offline training of the convolutional recurrent autoencoder in more detail. This model was built and trained using the open-source deep learning library TensorFlow⁵⁷.

Algorithm 4.1: Convolutional Recurrent Autoencoder Training Algorithm

Input: Training dataset $\mathcal{X} \in [0, 1]^{N_x \times N_y \times N_t \times N_s}$, number of train-steps N_{train} , batch size N_b .

Result: Trained model parameters θ

```

1 Randomly initialize  $\theta$ ;
2 for  $i \in \{1, \dots, N_{train}\}$  do
3   Randomly sample batch from training data:  $\mathcal{X}^b \subset \mathcal{X}$ ;
4   Flatten batch-mode:  $\mathcal{X}^{b_{AE}} \leftarrow \text{flatten}(\mathcal{X}^b)$  s.t.  $\mathcal{X}^{b_{AE}} \in [0, 1]^{N_x \times N_y \times (N_t \cdot N_b)}$ ;
5   Encoder forward pass:  $\tilde{\mathcal{H}}^b \leftarrow f_{enc}(\mathcal{X}^{b_{AE}})$  where  $\tilde{\mathcal{H}}^b \in \mathbb{R}^{N_h \times (N_t \cdot N_b)}$ ;
6   Decoder forward pass:  $\hat{\mathcal{X}}^{b_{AE}} \leftarrow f_{dec}(\tilde{\mathcal{H}}^b)$ ;
7   Reshape low-dimensional features:  $\mathcal{H}^b \in \mathbb{R}^{N_h \times N_t \times N_b} \leftarrow \text{reshape}(\tilde{\mathcal{H}}^b)$ ;
8   Initialize RNN subgraph loop:  $\hat{\mathbf{h}}_i^2 \leftarrow f_{LSTM}(\mathbf{h}_i^1)$  for  $i \in \{1, \dots, N_b\}$ ,  $\mathbf{h}_i^1 \subset \mathcal{H}^b$ ;
9   for  $n \in \{2, \dots, N_t - 1\}$  do
10     $\hat{\mathbf{h}}_i^{n+1} \leftarrow f_{LSTM}(\hat{\mathbf{h}}_i^n)$  for  $i \in \{1, \dots, N_b\}$ ,  $\hat{\mathbf{h}}_i^n \subset \hat{\mathcal{H}}^b$ ;
11  end
12  Using  $\mathcal{X}^b$ ,  $\hat{\mathcal{X}}^b$ ,  $\mathcal{H}^b$ , and  $\hat{\mathcal{H}}^b$  calculate approximate gradient  $\hat{\mathbf{g}}$  of Equation 30;
13  Update parameters:  $\theta \leftarrow ADAM(\hat{\mathbf{g}})$ 
14 end
```

Once the model is trained, online prediction is straightforward. Using the trained parameters θ^* , and given an initial condition $\mathbf{x}^0 \in [0, 1]^{N_x \times N_y}$, a low-dimensional representation of the initial condition $\mathbf{h}^0 \in \mathbb{R}_h^N$ is constructed using the encoder network. Iterative applications of Equation 25 are then used to evolve this low-dimensional representation for N_t steps. The modular construction of the convolutional recurrent autoencoder model allows the user to reconstruct from $\hat{\mathbf{h}}^n$ the full-dimensional state $\hat{\mathbf{x}}^n$ at every time step or at any specific instance. The online prediction algorithm is outlined in Algorithm 4.2.

Algorithm 4.2: Convolutional Recurrent Autoencoder Prediction Algorithm

Input: Initial condition $\mathbf{x}^0 \in [0, 1]^{N_x \times N_y}$, number of prediction steps N_t .

Result: Model prediction $\hat{\mathbf{X}} = [\hat{\mathbf{x}}^1, \dots, \hat{\mathbf{x}}^{N_t}] \in [0, 1]^{N_x \times N_y \times N_t}$.

```

1 Load trained parameters  $\theta^*$ ;
2 Encoder forward pass:  $\mathbf{h}^0 \leftarrow f_{enc}(\mathbf{x}^0)$ ;
3 Initialize RNN subgraph loop:  $\hat{\mathbf{h}}^1 \leftarrow f_{LSTM}(\mathbf{h}^0)$ ;
4 for  $n \in \{1, \dots, N_t - 1\}$  do
5   |  $\hat{\mathbf{h}}^{n+1} \leftarrow f_{LSTM}(\hat{\mathbf{h}}^n)$ ;
6 end
7 Decoder forward pass:  $\hat{\mathbf{X}} \leftarrow f_{dec}(\hat{\mathbf{H}})$ , where  $\hat{\mathbf{H}} = [\hat{\mathbf{h}}^1, \dots, \hat{\mathbf{h}}^{N_t}]$ ;

```

5 | NUMERICAL EXPERIMENTS

We apply the methods described in the previous sections on three representative examples to illustrate the effectiveness of deep autoencoder-based approaches to nonlinear model reduction. The first one considers only a 4-layer fully-connected recurrent autoencoder model applied to a simple one-dimensional problem based on the viscous Burgers equation. This has the merit of demonstrating the performance of autoencoders equipped with nonlinear activation functions on tasks where linear methods tend to struggle. The second example considers a parametric model reduction problem based on two-dimensional fluid flow in a periodic domain with significant parameter variations. In this case, our convolutional recurrent autoencoder model is tasked with predicting new solutions given new parameters (i.e., parameters unseen during training). The third example focuses on long-term prediction of an incompressible flow inside a lid-driven cavity. This case serves to highlight the long-term stability and overall performance of the convolutional recurrent autoencoder model in contrast to the unstable behavior exhibited by POD-Galerkin ROMs.

5.1 | Viscous Burgers equation

First, we consider the one-dimensional viscous Burgers equation given by

$$\begin{aligned}
 \frac{\partial u}{\partial t} + u \frac{\partial u}{\partial x} &= \frac{1}{Re} \frac{\partial^2 u}{\partial x^2}, \quad (x, t) \in [0, L] \times [0, T], \\
 u(x, 0) &= 1 + \exp\left(-\frac{2(x - x_0)^2}{0.1^2}\right), \\
 u(0, t) &= 0,
 \end{aligned} \tag{31}$$

where $L = 1.5$, $T = 0.3$, x_0 is the initial location of the Gaussian initial condition, and the Reynolds-like number is set to $Re = 200$. This problem is spatially discretized onto a uniform $N_x = 1024$ grid using a second order finite difference scheme with a grid spacing of $\Delta x = L/N_x$. A parameter-varying dataset consisting of $N_s = 128$ training samples is created by randomly sampling $x_0 \in [0, L]$ and solving Equation 31 using a fourth-order Runge-Kutta scheme with $\Delta t = 0.5\Delta x$. After subtracting the mean and feature scaling each solution snapshot, the training dataset has the form of Equation 28 where each training sample is a matrix of solution snapshots $\mathbf{X}_s^i = [\mathbf{u}_{s,i}^1, \dots, \mathbf{u}_{s,i}^{N_t}] \in \mathbb{R}^{N_x \times N_t}$ and corresponds to a different initial condition x_0^i . In this case, $N_t = 40$ is the number of equally spaced snapshots sampled from each trajectory.

This example was crafted to highlight an important performance benefit of using nonlinear fully-connected autoencoder-based model reduction approaches in contrast to POD-based ROMs. First, we train a 4-layer fully-connected autoencoder (2 encoder layers and 2 decoder layers) to produce a low-dimensional representation $\mathbf{h}_{AE} \in \mathbb{R}^{N_h}$, $N_h = 20$ with intermediate layer of size 512. The evolution of this representation and an equivalently sized optimal POD representation $\mathbf{h}_{POD} = \Psi_{N_h}^T \mathbf{u}_s'$ are both modeled using separate single layer modified LSTM networks trained according to a simplified version of Algorithm 4.1 using a batch size $N_b = 8$. A best-case scenario for any POD-based ROM are snapshot reconstructions satisfying Equation 12, therefore in lieu of a POD-Galerkin-ROM we will consider only the projected solution snapshots. These proof-of-concept models were each trained over $N_{train} = 100,000$ iterations on a desktop computer in a matter of minutes.

Figure 5 depicts the comparison between exact solution, the best-case optimal POD reconstruction, the POD-LSTM reconstruction, and finally the shallow recurrent autoencoder reconstruction. As expected, due to the truncation of higher-frequency

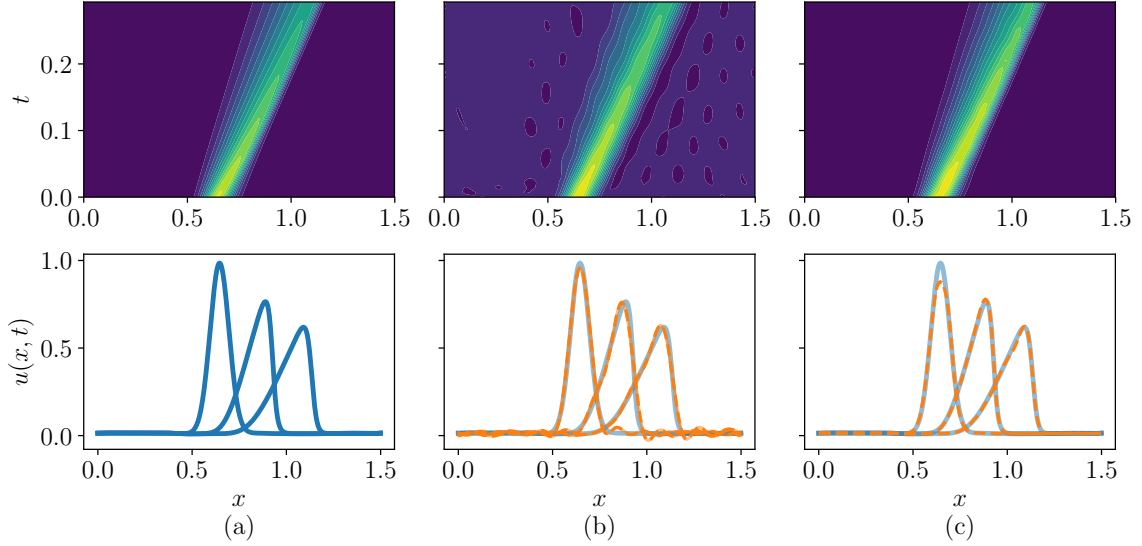


FIGURE 5 (a) exact solution, (b) $N_h = 20$; L_2 -optimal POD reconstruction (solid orange), POD-LSTM reconstruction (dashed orange), exact solution (light blue), (c) $N_h = 20$; shallow autoencoder-LSTM reconstruction (dashed orange), exact solution (light blue).

POD modes the L_2 -optimal POD reconstruction exhibits spurious oscillations. The spurious oscillations, aside from signifying a poor reconstruction, may lead to stability issues in POD-Galerkin ROMs. This is widely known to be a problem for model reduction of fluid flows where POD-Galerkin ROMs, while capturing nearly all the energy of the system truncate low-energy modes which can have a large influence on the dynamics. Additionally, in agreement with similar work in ^{10,12}, the POD-LSTM model was able to accurately capture the evolution of the optimal POD representation in a non-intrusive manner.

More importantly, the power of recurrent autoencoder-based approaches for nonlinear model reduction is exhibited in the reconstruction using the shallow recurrent autoencoder model. The effect of nonlinearities in the fully-connected autoencoder help to identify a more expressive low-dimensional representation of the full state. Combining this with an LSTM network to evolve these low-dimensional representations yields an effective nonlinear reduced order modeling approach that outperforms best-case scenario POD-based ROMs while using the same size models.

5.2 | Parameter-varying flow in a periodic box

Next we will consider the problem of a two-dimensional incompressible flow in a square periodic domain prescribed by the Navier-Stokes equations in vorticity formulation

$$\frac{\partial \omega}{\partial t} + \mathbf{u} \cdot \nabla \omega = \frac{1}{\text{Re}} \nabla^2 \omega, \quad (32)$$

defined on the domain $(x, y) = [0, 2\pi] \times [0, 2\pi]$ where $\omega(x, y, t)$ is the vorticity field, $\mathbf{u}(x, y, t)$ is the velocity vector field. The Reynolds number is set to $\text{Re} = 5 \times 10^3$. For the construction of the dataset, we will consider a family of initial conditions given by a mixture of N_v Gaussian vortices

$$\omega(x, y, 0) = \sum_{i=1}^{N_v} \delta(i) \exp \left(-\frac{(x - x_i)^2 + (y - y_i)^2}{0.1} \right), \quad (33)$$

parameterized by location of the center of each vortex. Each vortex center is sampled randomly from a square subdomain $(x_i, y_i) \in [\pi/2, 3\pi/2] \times [\pi/2, 3\pi/2] \forall i$ as depicted in Figure 6, and the sign of each vortex is governed by $\delta(i) \in \{-1, +1\} \forall i$. We consider two cases: (a) $N_v = 2$, with each vortex of opposite sign, and (b) $N_v = 3$, with one positive vortex and the rest negative. A representative set of initial conditions for the $N_v = 2$ and $N_v = 3$ cases can be seen in Figure 7 and Figure 8, respectively. This example was constructed both to showcase the application to larger scale problems that would otherwise be too computationally intensive using a fully-connected autoencoder and to highlight the location-invariance capabilities of the

convolutional autoencoder. The main idea is that similar to detecting an instance of an object anywhere in an image, the shared-weight property of each convolutional layer in the autoencoder should be able to capture the large-parameter variations implicitly defined in the initial condition.

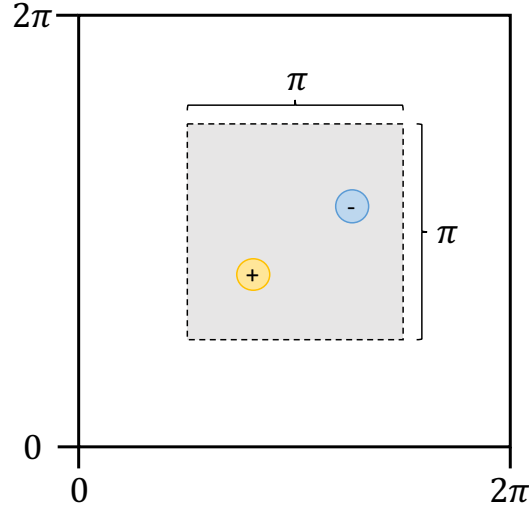


FIGURE 6 Square domain with periodic boundary conditions. The positive and negative vortices of equal strength are randomly initialized within the grey subdomain.

To create a training dataset, Equation 32 is discretized pseudospectrally using a uniform 128^2 grid and integrated in time using the Crank-Nicholson method to $T = 250$ using a time step of $\Delta t = 1 \times 10^{-2}$. A parameter-varying dataset is created by randomly sampling the initial Gaussian center locations from a square subdomain as was previously described. Similar to first example, after subtracting the temporal mean and feature scaling the resulting dataset has the form

$$\mathcal{X} = \{\mathbf{X}_s^1, \dots, \mathbf{X}_s^{N_s}\} \in [0, 1]^{N_x \times N_y \times N_t \times N_s}, \quad (34)$$

where each training sample $\mathbf{X}_s^i = [\boldsymbol{\omega}_{s,i}^1, \dots, \boldsymbol{\omega}_{s,i}^{N_t}]$ is a matrix of two-dimensional discretized snapshots corresponding to a different set of initial conditions. In this case, the dataset consists of a total $N_s = 5120$ training samples, each with $N_t = 30$ evenly sampled snapshots. Since we are interested in employing the convolutional recurrent autoencoder, each $\boldsymbol{\omega}_{s,i}^t$ is kept as a two-dimensional array.

Three convolutional recurrent autoencoder models, with feature vector sizes $N_h = 8, 16$, and 64 , were trained using the dataset Equation 34 with both two and three initial vortices. Each model was trained on an single Nvidia Tesla K20 GPU for $N_{train} = 1,000,000$ iterations. Once trained, the three models were used to predict the evolution of the vorticity field for new initial conditions. To highlight the benefits of convolutional recurrent autoencoders for location-invariant feature learning, we compare our prediction with a set of best-case scenario rank-8 POD reconstructions. These rank-8 POD reconstructions use a dataset containing snapshots from just 128 separate trajectories. In this case, a rank-8 POD reconstruction is not sufficient to accurately capture the correct solution since the inclusion of randomly varying initial conditions has created a dataset that is no longer low-rank. This is clearly shown in Figure 9 and Figure 10 for the two and three vortex cases. The need for more and more POD modes to achieve a good reconstruction underscores a significant disadvantage of POD-based ROMs for systems with large variations in parameters. The convolutional recurrent autoencoder overcomes these challenges and performs well in prediction new solutions without the need to resort to larger-rank models. In contrast to POD-Galerkin ROMs, increasing the number of separate trajectories in a dataset is beneficial to learning the correct dynamic behavior.

Similar to the first numerical example, the predictions are devoid of any spurious oscillations that are commonplace in POD-based ROMs. Considering a single initial condition Figure 11 shows the performance of each sized model in predicting the location of each vortex as it evolves up to the training sequence length for the two vortex case. Further, Figure 12 shows the

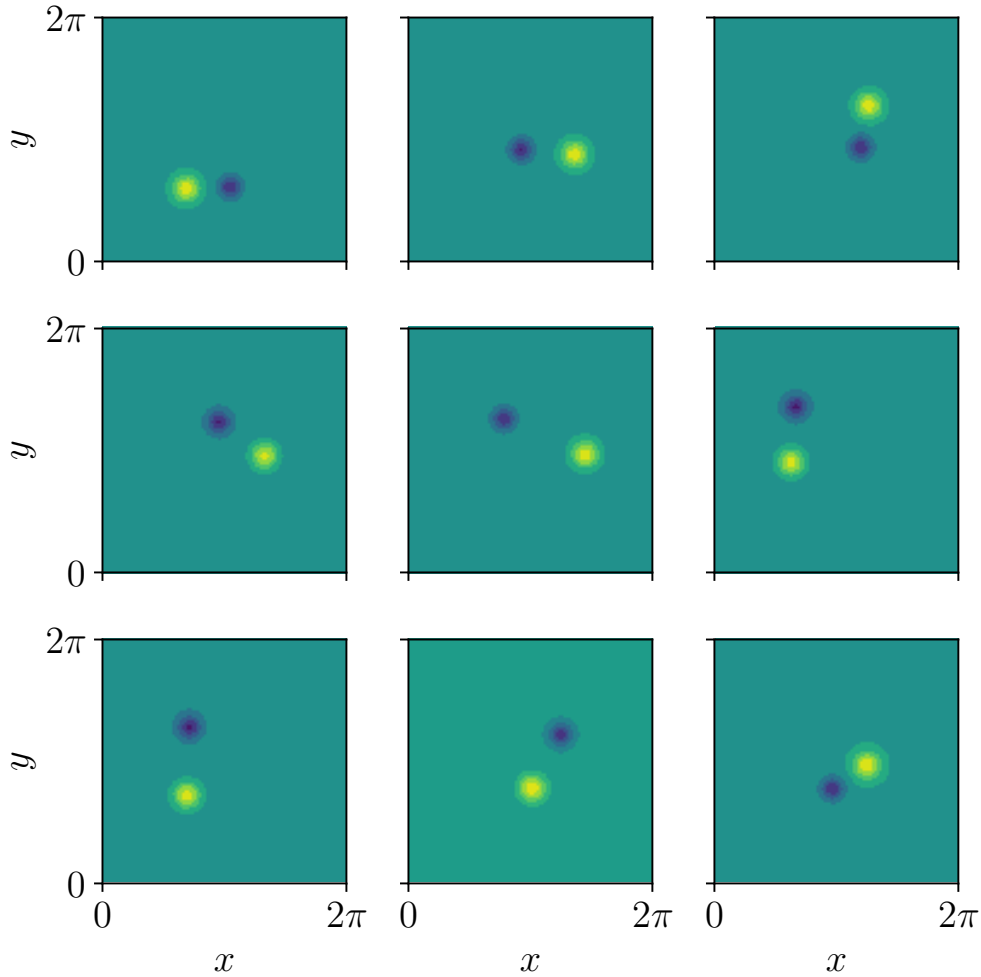


FIGURE 7 A set of initial conditions with two randomly located Gaussian vortices of equal and opposite strength.

mean and standard deviation of the scaled squared reconstruction error

$$\frac{\|\boldsymbol{\omega}'^n - \hat{\boldsymbol{\omega}}_s'^n\|_F^2}{\|\boldsymbol{\omega}'^n\|_F^2 + \epsilon} \quad (35)$$

at each time step as calculated from 512 new prediction runs using the trained models. In all three cases, the error did not grow significantly over the length of the training sequence.

5.3 | Lid-driven cavity flow

In the final example we consider a two-dimensional incompressible flow inside a square cavity with a lid velocity of $\mathbf{u}_{\text{lid}} = (1 - x^2)^2$ at a moderate Reynolds number $\text{Re} = 2.75 \times 10^4$. A graphic of the domain is depicted in Figure 13. At these Reynolds numbers the lid-driven cavity flow is known to settle into a statistically stationary solution far from the initial condition making it a well known benchmark for the validation of numerical schemes and reduced order models. In particular, this benchmark is useful for testing the stability of reduced order models²⁵. The characteristic length and velocity scales used in defining the Reynolds number are the cavity width and the maximum lid velocity.

Consider the two-dimensional Navier-Stokes in streamfunction-vorticity formulation defined on the square domain $(x, y) \in [-1, 1] \times [-1, 1]$

$$\frac{\partial}{\partial t}(\nabla^2 \Psi) + \frac{\partial \Psi}{\partial y} \frac{\partial}{\partial x}(\nabla^2 \Psi) - \frac{\partial \Psi}{\partial y} \frac{\partial}{\partial y}(\nabla^2 \Psi) = \nu \nabla^4 \Psi, \quad (36)$$

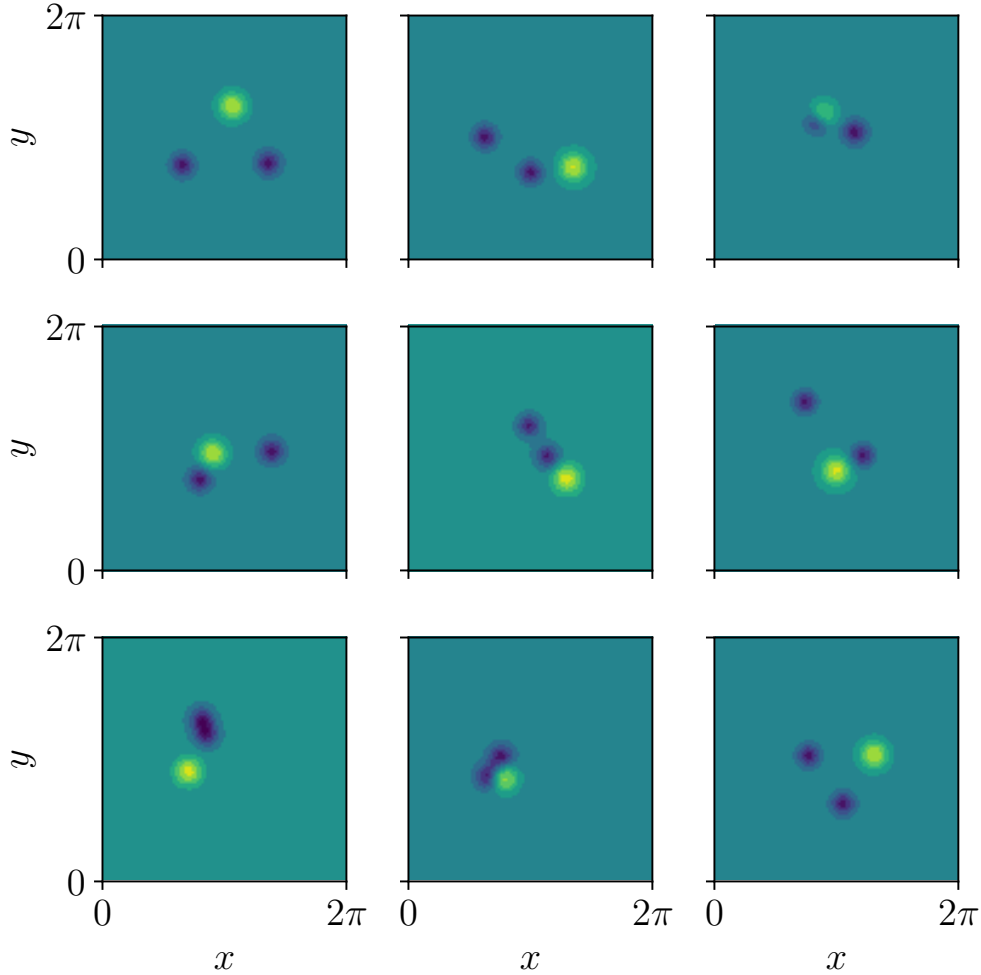


FIGURE 8 A set of initial conditions with three randomly located Gaussian vortices, one positive and two negative all with equal strength.

where $\Psi(x, y, t)$ is the streamfunction, and $\nabla^4 = \nabla^2 \nabla^2$ is the biharmonic operator. To generate the training dataset, Equation 36 is spatially discretized using a 128^2 Chebyshev grid and solved numerically. The Chebyshev coefficients are derived using the fast Fourier transform (FFT), where the contractive nonlinearities are handled pseudospectrally. The equations are integrated in time using a semi-implicit, second order Euler scheme. Since the statistically stationary solution is far from the initial condition, we first initialize the simulation over 7,500,000 time steps with time-step size $\Delta t = 1 \times 10^{-4}$. The following 2,500,000 time steps are then used to create a dataset in the form of Equation 28 with $N_s = 1110$ where now each training sample is

$$\mathbf{X}_s^i = [\Psi_s^i, \Psi_s^{i+m}, \Psi_s^{i+2m}, \dots, \Psi_s^{i+(N_t-1)m}] \in \mathbb{R}^{N_x \times N_y \times N_t}, \quad (37)$$

where each Ψ_s^i is a discretized two-dimensional snapshot of Equation 36, $N_t = 35$, and m is taken to be 100. In doing this, we ensure that the initial training snapshot used to initialize the RNN portion of the model evenly samples the entire trajectory of Equation 36. The result is the construction a training dataset that gives a good representation of the dynamics for the RNN to learn. In addition, an interpolation step onto a uniform 128^2 is performed to ensure each filter \mathbf{K}^f acts on equally physically-sized receptive fields.

Three convolutional recurrent autoencoder models were trained using this dataset, again with low-dimensional representations of sizes $N_h = 8, 16$, and 64 . In this case all three models were trained on a single Nvidia Tesla K20 GPU for $N_{train} = 600,000$ iterations. The online performance of the each model was evaluated by initializing each model with a slightly perturbed version of the first snapshot of the entire dataset and evaluating for 2500 prediction steps, over 70 times the length of each training sequence. We perform the same with three equivalently sized POD-Galerkin ROMs. ?? depict the final predicted velocity fields

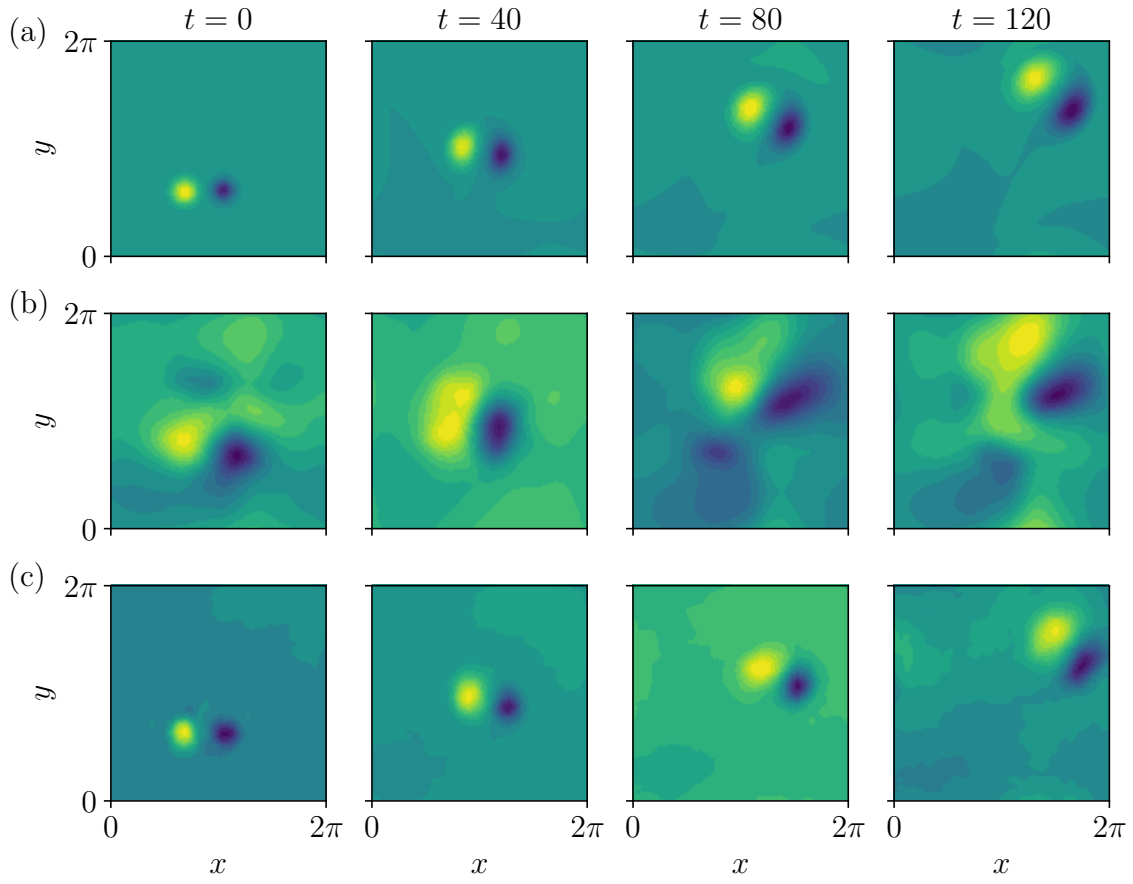


FIGURE 9 Comparison at $t = 0, 40, 80, 120$ of a sample trajectory using two initial vortices: (a) true solution, (b) rank-8 POD reconstruction using dataset with 128 trajectories, and (c) *prediction* using a trained convolutional recurrent autoencoder of size $N_h = 8$.

$u(x, y, t)$, $v(x, y, t)$, as well as the predicted vorticity field $\omega(x, y, t)$ using traditional POD-Galerkin ROMs and our convolutional recurrent autoencoder model for $N_h = 8, 16$, and 64 . In all three reconstructed fields the poor performance of POD-Galerkin ROMs can be easily noticed by the spurious oscillations present in the field. This is in contrast to the predictions presented using our approach, which nearly capture the exact solution even after long-term prediction.

In fact, we only present predictions up until $t = 60$ for the $N_h = 8$ POD-Galerkin ROM since instabilities cause the solution to diverge. This can be seen more clearly in Figure 17, which compares the instantaneous turbulent kinetic energy (TKE) of the flow

$$E(t) = \frac{1}{2} \int_{\Omega} \left(u(t)^{\prime 2} + v(t)^{\prime 2} \right) d\Omega \quad (38)$$

where $u(t)'$ and $v(t)'$ are the instantaneous velocity fluctuations around the mean and Ω represents the fluid domain. The TKE can be seen as a measure of the energy content within the flow. For statistically stationary flows, such as the one considered in this example, the TKE should hover around a mean value. In Figure 17 we see that the POD-Galerkin models fail to capture the correct TKE, and in the case of $N_h = 8$ instabilities lead to eventual divergence.

Against this backdrop, we can see that our approach vastly outperforms traditional POD-Galerkin ROMs. All velocity and vorticity reconstructions are in good agreement with the HFM solution. As the size of the model increases to $N_h = 64$, we see that predicted TKE is in good agreement with that of the HFM. It should be noted that the lid-driven cavity flow at these Reynolds numbers exhibits chaotic motion, thus a best-case scenario would be to capture the right TKE in a statistical sense. This can be seen further in Figure 18 which compares the power spectral density of each predicted TKE with that of the HFM.

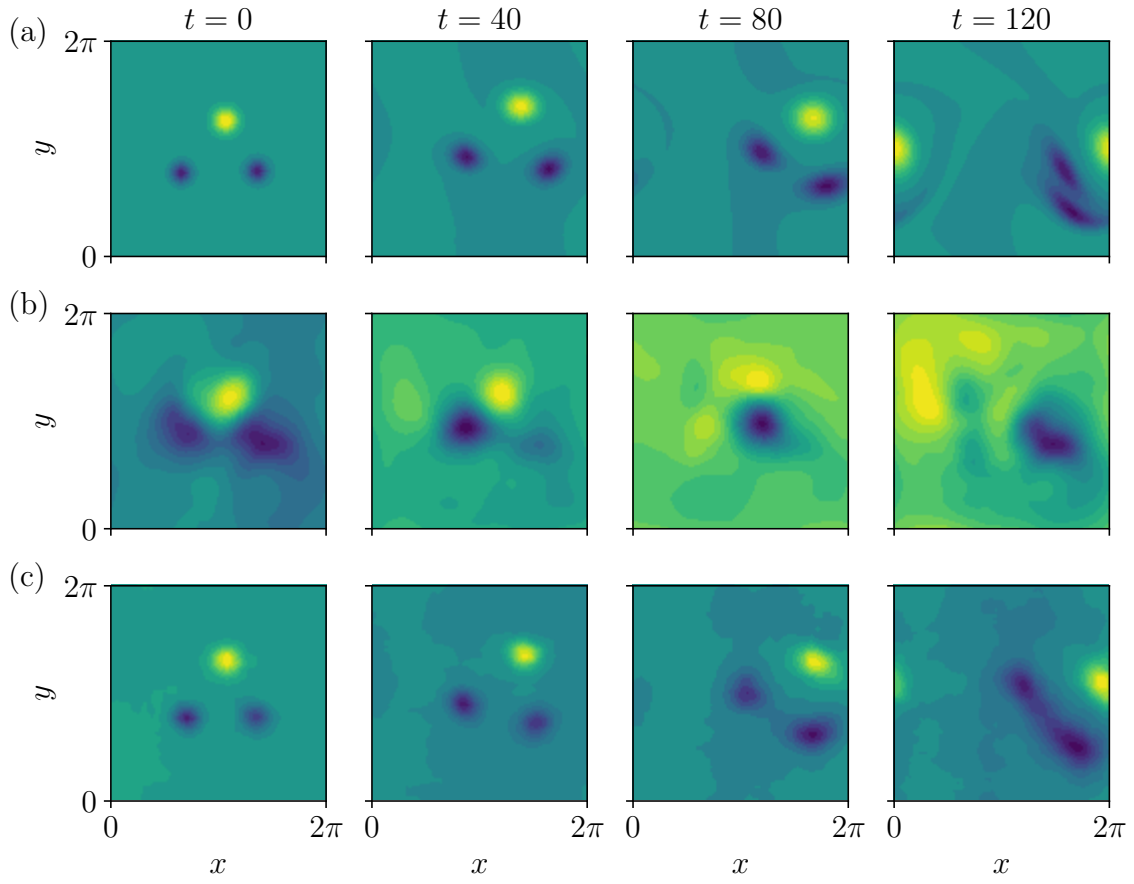


FIGURE 10 Comparison at $t = 0, 40, 80, 120$ of a sample trajectory using three initial vortices: (a) true solution, (b) rank-8 POD reconstruction using dataset with 128 trajectories, and (c) *prediction* using a trained convolutional recurrent autoencoder of size $N_h = 8$.

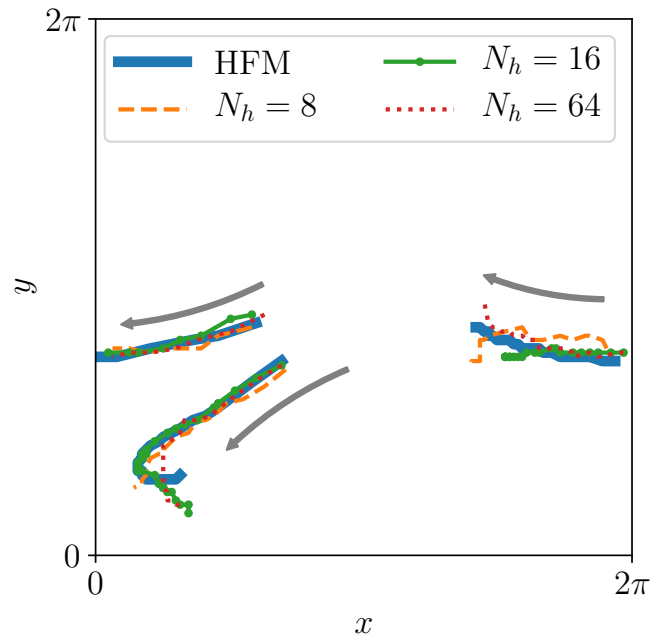


FIGURE 11 Evolution of the vortex centers as given the HFM solution and the predicted solutions using $N_h = 8, 16, 64$.

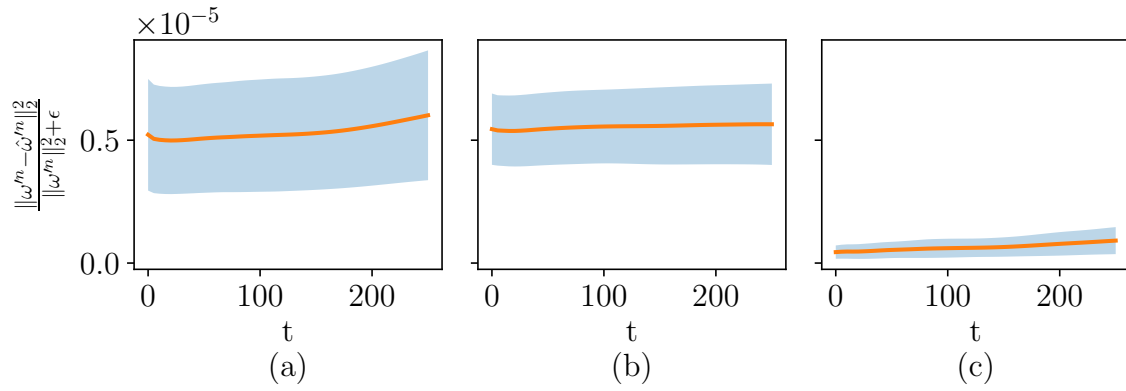


FIGURE 12 Mean and standard deviation of error at every time step for online predictions using (a) $N_h = 8$, (b) $N_h = 16$, and (c) $N_h = 64$.

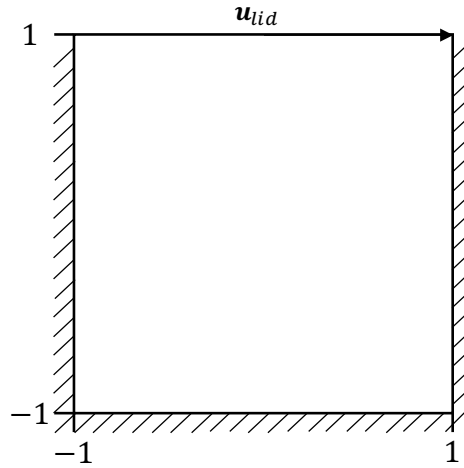


FIGURE 13 Lid-driven cavity domain, with lid velocity $\mathbf{u}_{\text{lid}} = (1 - x^2)^2$.

While each model prediction captures the general behavior of the HFM, there is some high spatial frequency error evident throughout the domain in each reconstruction. Interestingly, the stability of the RNN portion of the each model remains unaffected by this high-frequency noise suggesting that it is due only to the transpose convolutional decoder. This is possibly a result of performing a strided transpose convolution at each layer of the decoder. It is possible and perhaps beneficial to include a final undilated convolutional layer with a single feature map to filter some of the high-frequency reconstruction noise.

6 | CONCLUSIONS

In this work we propose a completely data-driven nonlinear reduced order model based on a convolutional recurrent autoencoder architecture for application to parameter-varying systems and systems requiring long-term stability. The construction of the convolutional recurrent autoencoder consists of two major components each of which performs a key task in projection based reduced order modeling. First a convolutional autoencoder is designed to identify a low-dimensional representation of two-dimensional input data in terms of intrinsic coordinates on some low-dimensional manifold embedded in the original, high-dimensional space. This is done by considering a 4-layer convolutional encoder which computes a hierarchy of localized, location invariant features that are passed to a two-layer fully connected encoder. The result of this is a mapping from the high-dimensional input space to a low-dimensional data-supporting manifold. An equivalent decoder architecture is considered for efficiently mapping from the low-dimensional representation to the original space. This can be intuitively understood

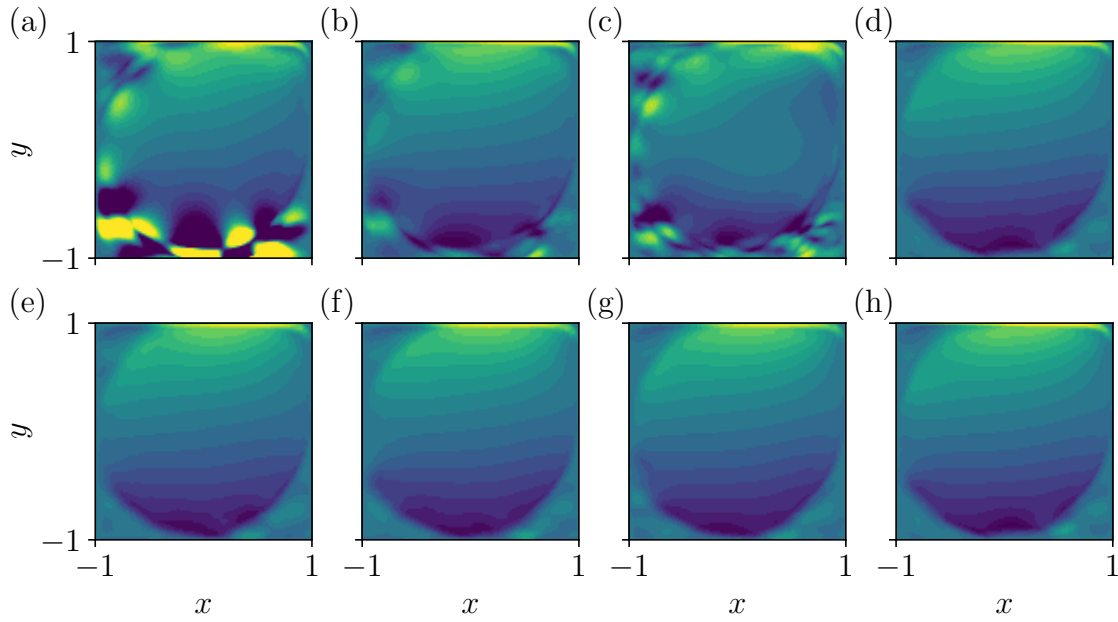


FIGURE 14 $u(x, y, t)$ contours of the lid-driven cavity flow at $t = 250$ s using the optimal POD reconstruction: (a) $N_h = 8$ (note: $t = 60$ shown, right before blowup), (b) $N_h = 16$, (c) $N_h = 64$, (d) true solution; and *predicted* contours using the convolutional recurrent autoencoder model with hidden state sizes (e) $N_h = 8$, (f) $N_h = 16$, (g) $N_h = 64$, (h) true solution.

as a nonlinear generalization of POD, where the structure of the manifold is more expressive than the linear subspaces learned by POD-based methods. The second important component of the proposed convolutional recurrent autoencoder is a modified version of an LSTM network which models the dynamics on the manifold learned by the autoencoder. The LSTM network is modified to require only information from the low-dimensional representation thereby avoiding costly reconstruction of the full state at every evolution step.

An offline training and online prediction strategy for the convolutional recurrent autoencoder is proposed in this work. The training algorithm exploits the modularity of the model by splitting each forward pass into two steps. The first step running a forward pass on the autoencoder while creating a temporary batch of target low-dimensional representations which are then used in the second step, which is the forward pass of the modified LSTM network. The backwards pass, or parameter update is then performed jointly equally weighting autoencoder reconstruction error and the prediction error of the modified LSTM network.

We demonstrated our approach on three illustrative nonlinear model reduction examples. The first emphasizes the expressive power of using fully-connected autoencoders equipped with nonlinear activation functions on performing model reduction tasks in contrast to POD-based methods. The second highlights the performance of the convolutional recurrent autoencoder, and in particular its location-invariant properties, in parametric model reduction with initial condition exhibiting large parameter variations. The final example demonstrates the stability of convolutional recurrent autoencoders when performing long-term predictions of chaotic incompressible flows. Collectively, these numerical examples show that our convolutional recurrent autoencoder model outperforms traditional POD-Galerkin ROMs both in terms of prediction quality, parameter variations, and stability while also offering other advantages such as location invariant feature learning and non-intrusiveness. In fact, although in this work we make use of canonical model reduction examples based on computational physics problems, our approach is completely general and can be applied to arbitrary high-dimensional spatiotemporal data. When compared to existing autoencoder-based reduced order modeling strategies, our model provides access to larger-sized problems while keeping the number of trainable parameters low compared to fully-connected autoencoders.

6.1 | Future work

This work shows the feasibility of using deep learning-based strategies for performing nonlinear model reduction and more generally modeling complex dynamical system in a completely data-driven and non-intrusive manner. Although this work presents

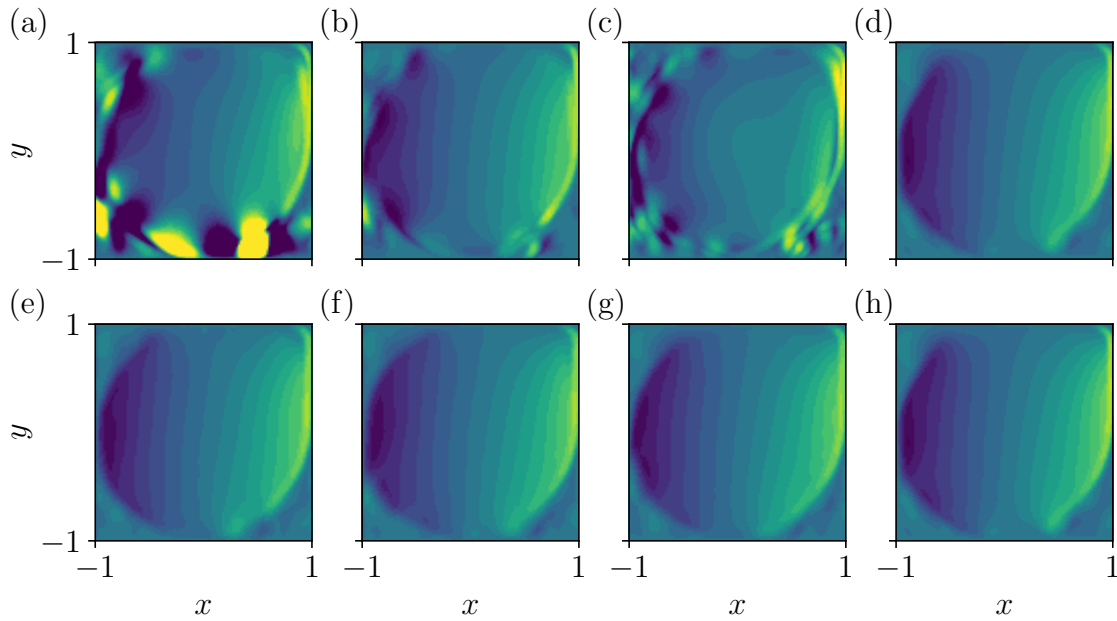


FIGURE 15 $v(x, y, t)$ contours of the lid-driven cavity flow at $t = 250$ s using the optimal POD reconstruction: (a) $N_h = 8$ (note: $t = 60$ shown, right before blowup), (b) $N_h = 16$, (c) $N_h = 64$, (d) true solution; and *predicted* contours using the convolutional recurrent autoencoder model with hidden state sizes (e) $N_h = 8$, (f) $N_h = 16$, (g) $N_h = 64$, (h) true solution.

promising predictive results for both parameter-varying model reduction problems and problems requiring long-term stability, these methods remain in their infancy and their full capabilities are yet unknown. There are multiple directions in which this work can be extended. One such direction is improving the design of the convolutional transpose decoder. As it stands, the main source of error in our results is high-frequency in nature and appears only during the decoding phase. Considering this, future decoder designs could include more efficient filtering strategies. Another possible direction is in the dynamic modeling of the low-dimensional representations. In this work, we considered samples with spatial parameter variations and thus the design of the LSTM network could remain unchanged. However, there is potential for deep learning-based dynamic modeling approaches that exploit multi-scale phenomena inherent in many physical systems. Finally, a much more challenging problem is the reconciliation of deep learning-based performance gains with physical intuition. This issue permeates throughout all fields where deep learning has made an impact: what is it actually doing? Developing our understanding of deep learning-based modeling strategies can potentially provide us with deeper insights of the dynamics inherent in a physical system.

ACKNOWLEDGMENTS

This material is based upon the work supported by the Air Force Office of Scientific Research under Grant No. FA9550-17-1-0203. Simulations and model training were also made possible in part by an exploratory award from the Blue Waters sustained-petascale computing project, which is supported by the National Science Foundation (awards OCI-0725070 and ACI-1238993) and the state of Illinois. Blue Waters is a joint effort of the University of Illinois at Urbana-Champaign and its National Center for Supercomputing Applications.

References

1. Raissi M, others . Machine learning of linear differential equations using Gaussian processes. *Journal of Computational Physics* 2017; 348: 683–693. doi: 10.1016/j.jcp.2017.07.050

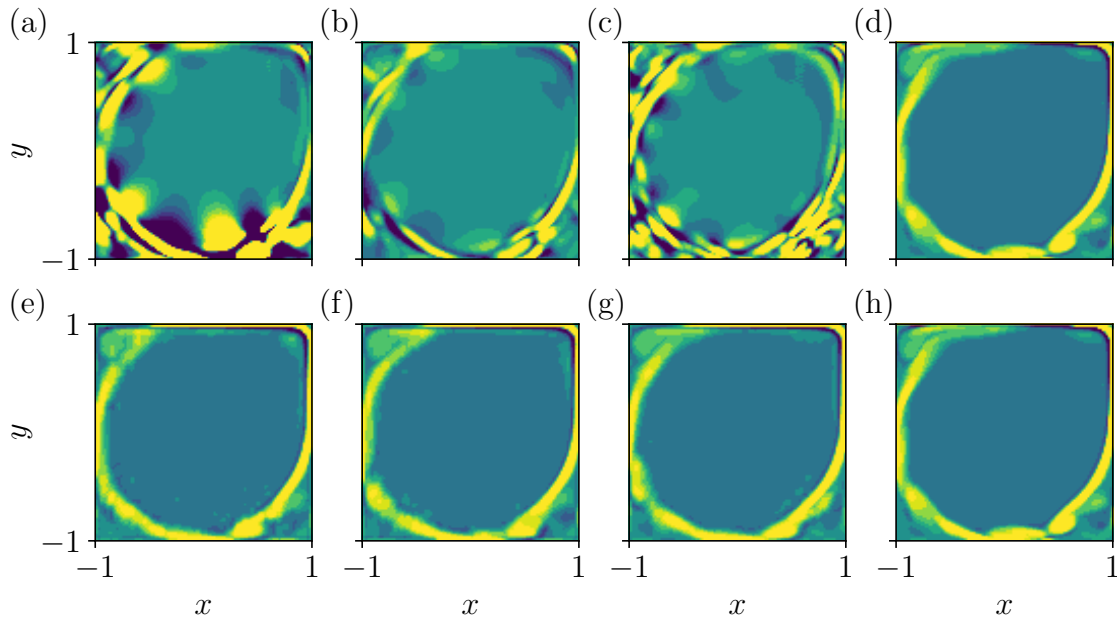


FIGURE 16 Vorticity contours of the lid-driven cavity flow at $t = 250$ s using the optimal POD reconstruction: (a) $N_h = 8$ (note: $t = 60$ shown, right before blowup), (b) $N_h = 16$, (c) $N_h = 64$, (d) true solution; and *predicted* contours using the convolutional recurrent autoencoder model with hidden state sizes (e) $N_h = 8$, (f) $N_h = 16$, (g) $N_h = 64$, (h) true solution.

2. Brunton SL, Brunton BW, Proctor JL, Kaiser E, Kutz JN. Chaos as an intermittently forced linear system. *Nature Communications* 2017; 8(1): 19. doi: 10.1038/s41467-017-00030-8
3. Bongard J, Lipson H. Automated reverse engineering of nonlinear dynamical systems. *Proceedings of the National Academy of Sciences* 2007; 104(24): 9943–9948. doi: 10.1073/pnas.0609476104
4. Schaeffer H. Learning partial differential equations via data discovery and sparse optimization. *Proceedings of the Royal Society A: Mathematical, Physical and Engineering Science* 2017; 473(2197): 20160446. doi: 10.1098/rspa.2016.0446
5. Tran G, Ward R. Exact Recovery of Chaotic Systems from Highly Corrupted Data. *Multiscale Modeling & Simulation* 2017; 15(3): 1108–1129. doi: 10.1137/16M1086637
6. Raissi M, Perdikaris P, Karniadakis GE. Inferring solutions of differential equations using noisy multi-fidelity data. *Journal of Computational Physics* 2016; 335: 736–746. doi: 10.1016/j.jcp.2017.01.060
7. Brunton SL, Proctor JL, Kutz JN. Discovering governing equations from data by sparse identification of nonlinear dynamical systems. *Proceedings of the National Academy of Sciences* 2016; 113(15): 3932–3937. doi: 10.1073/pnas.1517384113
8. San O, Maulik R. Neural network closures for nonlinear model order reduction. 2017; 1(405): 1–33.
9. Benosman M, Borggaard J, San O, Kramer B. Learning-based robust stabilization for reduced-order models of 2D and 3D Boussinesq equations. *Applied Mathematical Modelling* 2017; 49: 162–181. doi: 10.1016/j.apm.2017.04.032
10. Wang Z, others . Model identification of reduced order fluid dynamics systems using deep learning. *International Journal for Numerical Methods in Fluids* 2017(July): 1–14. doi: 10.1002/fld.4416
11. Wang Q, Hesthaven JS, Ray D. Non-intrusive reduced order modeling of unsteady flows using artificial neural networks with application to a combustion problem. 2018.
12. Kani JN, Elsheikh AH. DR-RNN: A deep residual recurrent neural network for model reduction. *arXiv* 2017.
13. Otto SE, Rowley CW. Linearly-Recurrent Autoencoder Networks for Learning Dynamics. *arXiv* 2017: 1–37.

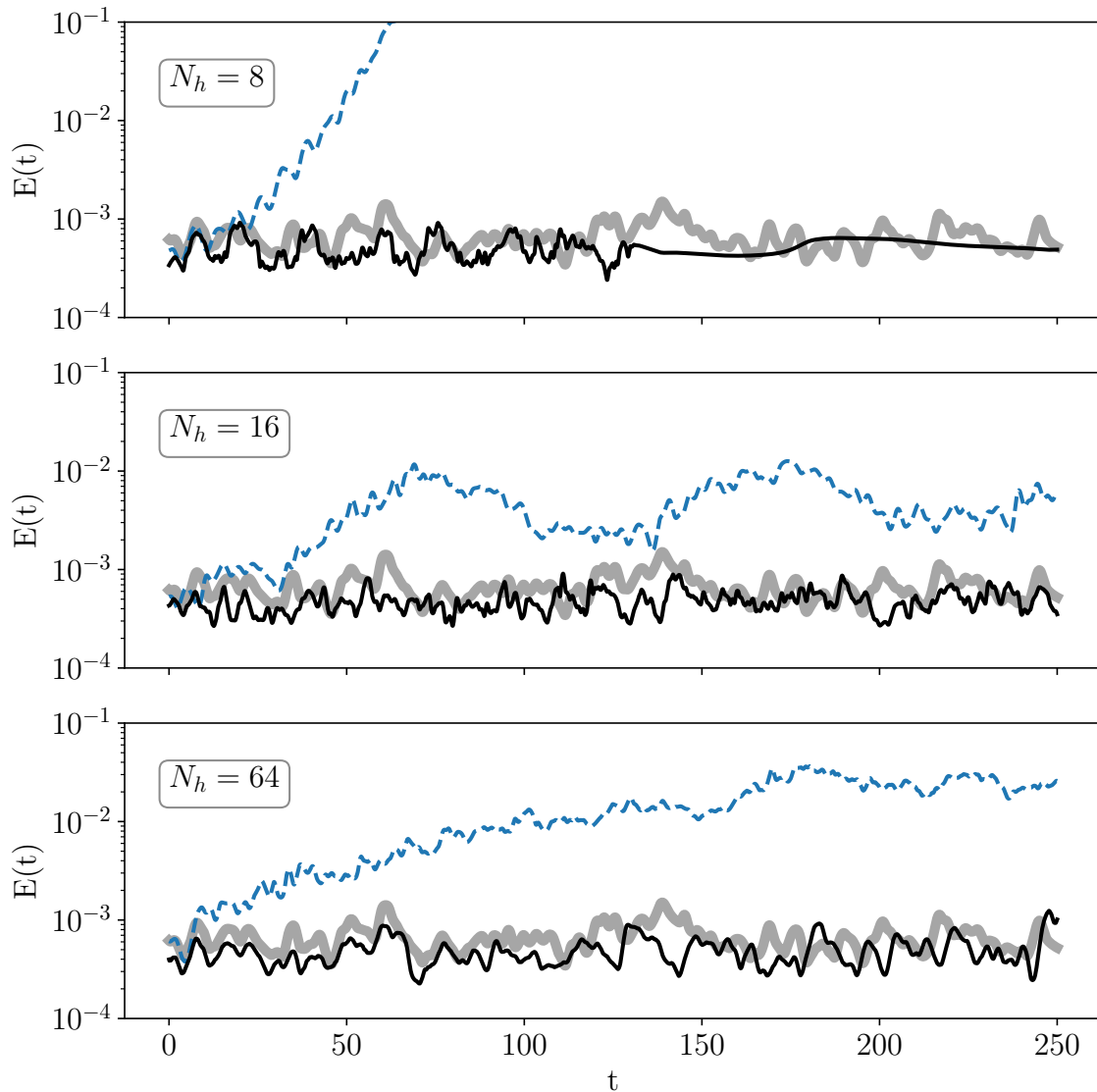


FIGURE 17 The evolution of the instantaneous turbulent kinetic energy for the lid-driven cavity flow from the DNS (thick grey lines), standard POD-based Galerkin ROMs (blue dashed lines), and our method (solid black lines).

14. Benner P, Gugercin S, Willcox K. A Survey of Projection-Based Model Reduction Methods for Parametric Dynamical Systems. *SIAM Review* 2015; 57(4): 483–531. doi: 10.1137/130932715
15. Carlberg K, Bou-Mosleh C, Farhat C. Efficient non-linear model reduction via a least-squares Petrov-Galerkin projection and compressive tensor approximations. *International Journal for Numerical Methods in Engineering* 2011; 86(2): 155–181. doi: 10.1002/nme.3050
16. Parish EJ, Duraisamy K. A paradigm for data-driven predictive modeling using field inversion and machine learning. *Journal of Computational Physics* 2016; 305: 758–774. doi: 10.1016/j.jcp.2015.11.012
17. Lumley JL. *Stochastic Tools in Turbulence*. Elsevier . 1970.
18. Holmes P, Lumley JL, Berkooz G. *Turbulence, Coherent Structures, Dynamical Systems and Symmetry*. Cambridge: Cambridge University Press . 1996
19. Bai Z. Krylov subspace techniques for reduced-order modeling of large-scale dynamical systems. *Applied Numerical Mathematics* 2002; 43(1-2): 9–44. doi: 10.1016/S0168-9274(02)00116-2

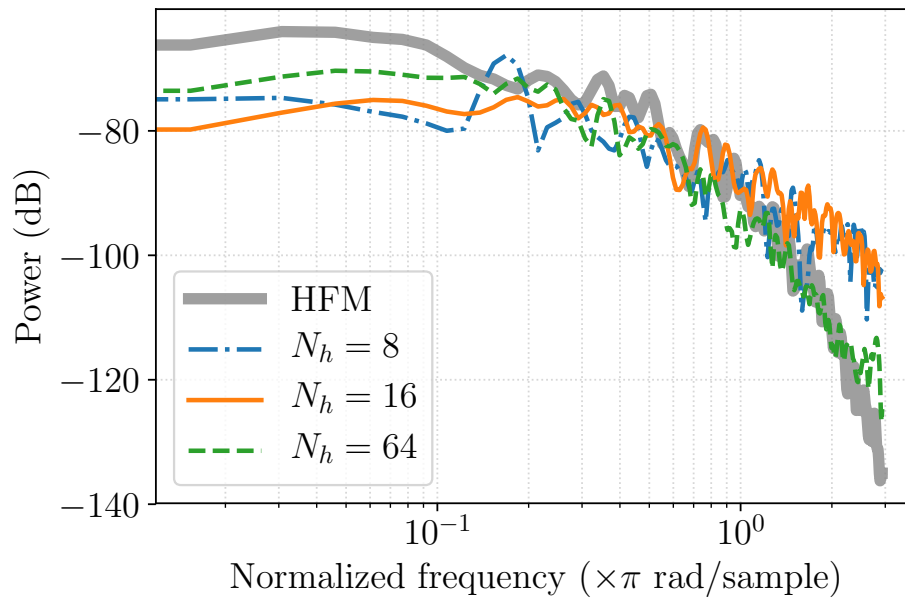


FIGURE 18 PSD of the turbulent kinetic energy of the lid-driven cavity flow.

20. Schmid PJ. Dynamic mode decomposition of numerical and experimental data. *Journal of Fluid Mechanics* 2010; 656: 5–28. doi: 10.1017/S0022112010001217
21. Chaturantabut S, Sorensen DC. Nonlinear Model Reduction via Discrete Empirical Interpolation. *SIAM Journal on Scientific Computing* 2010; 32(5): 2737–2764. doi: 10.1137/090766498
22. Carlberg K, Farhat C, Cortial J, Amsallem D. The GNAT method for nonlinear model reduction: Effective implementation and application to computational fluid dynamics and turbulent flows. *Journal of Computational Physics* 2013; 242: 623–647. doi: 10.1016/j.jcp.2013.02.028
23. Rewieński M, White J. Model order reduction for nonlinear dynamical systems based on trajectory piecewise-linear approximations. *Linear Algebra and its Applications* 2006; 415(2-3): 426–454. doi: 10.1016/j.laa.2003.11.034
24. Trehan S, Durlofsky LJ. Trajectory piecewise quadratic reduced-order model for subsurface flow, with application to PDE-constrained optimization. *Journal of Computational Physics* 2016; 326: 446–473. doi: 10.1016/j.jcp.2016.08.032
25. Balajewicz MJ, Dowell EH, Noack BR. Low-dimensional modelling of high-Reynolds-number shear flows incorporating constraints from the Navier–Stokes equation. *Journal of Fluid Mechanics* 2013; 729: 285–308. doi: 10.1017/jfm.2013.278
26. Hinton GE. Reducing the Dimensionality of Data with Neural Networks. *Science* 2006; 313(5786): 504–507. doi: 10.1126/science.1127647
27. Wang Y, Yao H, Zhao S. Auto-encoder based dimensionality reduction. *Neurocomputing* 2016; 184: 232–242. doi: 10.1016/j.neucom.2015.08.104
28. Hartman D, Mestha LK. A Deep Learning Framework for Model Reduction of Dynamical Systems. In: ; 2017: 1917–1922.
29. Krizhevsky A, Sutskever I, Hinton GE. ImageNet Classification with Deep Convolutional Neural Networks. *Advances In Neural Information Processing Systems* 2012: 1–9.
30. Farabet C, Couprie C, Najman L, LeCun Y. Learning Hierarchical Features for Scene Labeling. *IEEE Transactions on Pattern Analysis and Machine Intelligence* 2013; 35(8): 1915–1929. doi: 10.1109/TPAMI.2012.231

31. Hinton G, others . Deep Neural Networks for Acoustic Modeling in Speech Recognition: The Shared Views of Four Research Groups. *IEEE Signal Processing Magazine* 2012; 29(6): 82–97. doi: 10.1109/MSP.2012.2205597
32. Xiong HY, others . The human splicing code reveals new insights into the genetic determinants of disease. *Science* 2015; 347(6218). doi: 10.1126/science.1254806
33. Leung MKK, Xiong HY, Lee LJ, Frey BJ. Deep learning of the tissue-regulated splicing code. *Bioinformatics* 2014; 30(12): i121–i129. doi: 10.1093/bioinformatics/btu277
34. Goodfellow I, Bengio Y, Courville A. *Deep Learning*. MIT Press . 2016.
35. LeCun Y, Bengio Y, Hinton G. Deep learning. *Nature* 2015; 521(7553): 436–444. doi: 10.1038/nature14539
36. Kingma DP, Ba J. Adam: A Method for Stochastic Optimization. *arXiv* 2014: 1–15.
37. Zeiler MD. ADADELTA: An Adaptive Learning Rate Method. *arXiv* 2012.
38. Rumelhart DE, Hinton GE, Williams RJ. Learning representations by back-propagating errors. *Nature* 1986; 323(6088): 533–536. doi: 10.1038/323533a0
39. Werbos P. Backpropagation through time: what it does and how to do it. *Proceedings of the IEEE* 1990; 78(10): 1550–1560. doi: 10.1109/5.58337
40. Bengio Y, Simard P, Frasconi P. Learning long-term dependencies with gradient descent is difficult. *IEEE Transactions on Neural Networks* 1994; 5(2): 157–166. doi: 10.1109/72.279181
41. Hochreiter S, Schmidhuber J. Long Short-Term Memory. *Neural Computation* 1997; 9(8): 1735–1780. doi: 10.1162/neco.1997.9.8.1735
42. Cho K, others . Learning Phrase Representations using RNN Encoder–Decoder for Statistical Machine Translation. In: Association for Computational Linguistics; 2014; Stroudsburg, PA, USA: 1724–1734
43. Yu F, Koltun V. Multi-Scale Context Aggregation by Dilated Convolutions. 2015. doi: 10.16373/j.cnki.ahr.150049
44. Li Y, Zhang X, Chen D. CSRNet: Dilated Convolutional Neural Networks for Understanding the Highly Congested Scenes. 2018. doi: 10.1109/CVPR.2018.00120
45. Bengio Y, Courville A, Vincent P. Representation Learning: A Review and New Perspectives. *IEEE Transactions on Pattern Analysis and Machine Intelligence* 2013; 35(8): 1798–1828. doi: 10.1109/TPAMI.2013.50
46. Plaut E. From Principal Subspaces to Principal Components with Linear Autoencoders. *arXiv* 2018: 1–6.
47. Ogunmolu O, Gu X, Jiang S, Gans N. Nonlinear Systems Identification Using Deep Dynamic Neural Networks. 2016.
48. Yeo K. Model-free prediction of noisy chaotic time series by deep learning. *arXiv* 2017(10): 1–5.
49. Li Q, Dietrich F, Bollt EM, Kevrekidis IG. Extended dynamic mode decomposition with dictionary learning: A data-driven adaptive spectral decomposition of the koopman operator. *Chaos* 2017; 27(10). doi: 10.1063/1.4993854
50. Clevert DA, Unterthiner T, Hochreiter S. Fast and Accurate Deep Network Learning by Exponential Linear Units (ELUs). 2015: 1–14. doi: 10.3233/978-1-61499-672-9-1760
51. Ma C, Huang Jb, Yang X, Yang Mh. Hierarchical Convolutional Features for Visual Tracking. In: IEEE; 2015: 3074–3082
52. Noh H, Hong S, Han B. Learning deconvolution network for semantic segmentation. *Proceedings of the IEEE International Conference on Computer Vision* 2015; 2015 Inter: 1520–1528. doi: 10.1109/ICCV.2015.178
53. Badrinarayanan V, Kendall A, Cipolla R. SegNet: A Deep Convolutional Encoder-Decoder Architecture for Image Segmentation. *IEEE Transactions on Pattern Analysis and Machine Intelligence* 2017; 39(12): 2481–2495. doi: 10.1109/TPAMI.2016.2644615

54. Lipton ZC, Berkowitz J, Elkan C. A Critical Review of Recurrent Neural Networks for Sequence Learning. *Proceedings of the ACM International Conference on Multimedia - MM '14* 2015: 675–678.
55. Sutskever I, Vinyals O, Le QV. Sequence to Sequence Learning with Neural Networks. *arXiv* 2014: 1–9.
56. Wu Y, others . Google’s Neural Machine Translation System: Bridging the Gap between Human and Machine Translation. *arXiv* 2016: 1–23. doi: abs/1609.08144
57. Abadi M, others . TensorFlow: A System for Large-Scale Machine Learning TensorFlow: A system for large-scale machine learning. *12th USENIX Symposium on Operating Systems Design and Implementation (OSDI '16)* 2016: 265–284. doi: 10.1038/n.3331

